

POLITECNICO DI TORINO

Corso di Laurea Magistrale in Ingegneria Elettronica

Tesi di Laurea Magistrale

Design of an Integrated Interferometric Biosensor for Silicon Photonics Technology



Relatore:

Prof. Paolo BARDELLA

Candidato:

Daniele SAVIO

ANNO ACCADEMICO 2020-2021

Aprile 2021

Abstract

The topic of my thesis work is the study of a family of optical biosensors based on Silicon technology. In the last decade this subject attracted the attention of academic and industrial researchers due to the need to develop new classes of devices able to perform in situ and real-time measurements at low cost together with the advancement in semiconductor micro fabrication technology.

Indeed the first part of the work is a review of the basic principles related to evanescent field sampling, namely an optical sensing mechanism based on the interaction between the evanescent tails of field confined in a waveguide and the target analyte. This family of Silicon-based optical sensors has a great appeal in many different fields, starting from the biomedical one to the control of liquid and gas quality in industry. As a matter of fact technological advancement in the semiconductor industry, which is now able to integrate in the same chip different type of sources and detectors together with their optical guiding structure, accommodates the needs of in situ and real-time measuring systems.

In the second part of my work, I explored the mole of already proposed architectures associated to the sense of variation in the refractive index and in the absorption spectrum, being among the commonest sensed physical quantities in this field. The former is commonly employing the standard SOI technology at $1.55\ \mu\text{m}$, whereas the latter can be based on different technologies and materials, being the spectroscopy often applied in the mid-infrared region where bio-molecules have their peculiar absorption fingerprints. Concerning the exploited architectures, interferometric and resonating structures are widely used in order to sense a variation in the refractive index. Starting from these basic building blocks many alternatives have been reported in the literature to increase the sensitivity of the sensors. This can be done at the architectural level, for example solutions can be found combining more than one cascaded ring resonator to exploit the Vernier effect. Furthermore, improvements can be made at the waveguide level. Indeed ultra-thin and slotted waveguide solutions are largely diffused in order to reduce the confinement of the field in the core and consequently increase the interaction in the cladding area. In spectroscopy on the other hand long (even up to 1 cm) folded waveguides are widely used to detect liquid and gaseous concentration even in the order of tens ppm.

Then, I focused my attention on the analysis and design of a Mid-Infrared imaging sensor in Silicon Photonics based on Optical Feedback Interferometry in the framework of an informal collaboration with Università di Bari and Politecnico di Bari. The problem treated in this thesis is to design an integrated device for raster scanning and single-pixel imaging. These techniques together with condensed sensing algorithm can have a great appeal in the bio-imaging field where, due to their limited dimensions, they can find application in

the tip of endoscopes. The key to condensed sensing is to have a source block able to illuminate the target with a pseudo-random pattern. Here I tried to design a system able to generate a controllable structured pattern starting from a standard multi-branch optical phase array (OPA), formed by a splitter, a phase-tuning region and a combiner. In particular, the optical radiation emitted from the laser source is sent to the $1 \times N$ splitter. At the output of each splitter channel, thermal tuning regions are used to selectively modify the optical path of each branch. The fields from the N waveguides are then recombined together and sent to the output.

The chosen technology was the standard SOI one with 220 nm overlayer. As extensively discussed in the thesis, the range of application of such technology in the infrared region is limited to the free-space wavelength of $4 \mu\text{m}$ due to the large absorption of Silica beyond that limit. The operating wavelength as a consequence is fixed to $4 \mu\text{m}$. For the numerical simulations associated to this design activity I exploited the commercial Rsoft Synopsys CAD [1].

I started with the analysis of the fundamental straight waveguide, with the determination of the optimal waveguide sizes to ensure that only the fundamental transverse mode is supported. To do that I took advantage of the FEMSim tool, a generalized mode solver based on the FEM. Then I focused my attention on the definition of the building blocks needed to implement the multi-branch OPA and started the optimization of each block separately. The phase-tuning was done exploiting the thermo-optical effect. Simulations on this complex effect were performed using the RSoft multi-physic tool, resolving the cross-sectional cut of a structure fixing the temperature of a component (see figure 3.8). In this step is optimized the distances between the branches to have good control on the phase-shift in each segment with minimal cross-talk, an important parameter in the definition of the splitter and combiner geometry. Moreover the length of this region is fixed to 1 mm once the wanted phase-shift and the phase-shift per unit length are defined. Subsequently I designed and optimized the 8 ports optical splitter. To do that I exploited the BEAMProp tool, a beam propagation method software. The best solution I found was a cascaded y-splitter with linear tapered region in correspondence of the split section, able to split the incoming power equally in eight branches with -1 dB losses (modal and bending losses) in approximately $500 \mu\text{m}$, with a final spacing of $25 \mu\text{m}$ needed for good individual thermal control.

Finally the combiner block was implemented using a MMI solution. The phase-shift signal coming from the different branches are combined in a tapered MMI (see figure 3.16) into an output multi-mode waveguide (having double width with respect to the normal one). The multi-mode output segment is the key for generating pseudo-random far field distributions required by the application I target in this thesis. While in the literature various solutions have been proposed to merge together the different fields after they have experienced the thermal tuned phase shift (such as using 1D to 2D converter to couple the integrated circuit to a multimode fiber), in this work I developed a solution integrated in the same plane obtaining promising results as the edge-emitted far field distribution exhibited by the combiner can be modified by controlling the phases of the inputs. The output field distribution can be controlled in terms of number, intensity and transverse dimension of the lobes (see figure 3.17). The correspondence between input phases and field intensity distribution was studied through a machine learning approach. This makes the designed multi-branch thermal-controlled OPA particularly well suited for condensed

imaging algorithm, where the shape of the target is reconstructed not by raster scan of the target itself but by illuminating it with a programmed series of pseudo-random field distribution to obtain faster results.

Acknowledgements

Ringrazio i miei genitori per avermi sostenuto nelle mie scelte durante questi lunghi 5 anni (e un po'). Ringrazio in maniera speciale mia sorella Elena per essermi stata accanto sempre e comunque e per avermi sostenuto in maniera speciale nell'ultimo anno. Per ultimi, ma non meno importanti, ringrazio i miei amici (Simone, Pietro, Marco, Matteo) per le ore spese 'in Gallia' e non solo.

Contents

List of Tables	9
List of Figures	10
1 Introduction	15
1.1 Motivations	15
1.1.1 Technology	15
1.1.2 Applications	16
1.1.3 Characteristic of a biosensor: figures of merit	17
1.2 Basic principles	17
1.2.1 Refractive index variation	18
1.2.2 Absorption spectroscopy	19
1.2.3 How to improve the architectures	22
1.2.4 Functionalization of the surface	25
2 State of the art of Silicon based biosensors	27
2.1 Sensors based on refractive index variations	27
2.1.1 MRR solutions	27
2.1.2 MZI solutions	30
2.2 Spectroscopy	34
3 Multi-branch OPA design and optimization	39
3.1 Materials and wavelength ranges selection	39
3.2 Dispersion relations of a waveguide	40
3.2.1 Waveguide design	44
3.3 Thermal control region	46
3.4 Optical splitter	48
3.5 Design of the MMI	50
3.5.1 Combiner	52
3.6 A Machine Learning approach to the coupler design and the control of far-field profile	57
3.7 Mask design	59

A	MATLAB programs	63
A.1	Dispersion relations of a slab waveguide and modal functions	63
A.2	Program to create the data-set for nanostructured splitter	66
A.3	Program to create the data-set for far-field study	69
A.4	Program for the training and testing of a NN for far-field computation . .	71
	Bibliography	73

List of Tables

3.1	Optimal values for the 1-to-4 splitter coming from MOST optimization in RSoft	49
3.2	Optimal values for the 1-to-8 splitter coming from MOST optimization in RSoft	51
3.3	Optimal values for the 1-to-2 MMI splitter coming from MOST optimization in RSoft.	52
3.4	Optimal values for the 1-to-4 MMI splitter coming from MOST optimization in RSoft.	53
3.5	Optimal values for the 8-to-1 MMI combiner with tapered width coming from MOST optimization in RSoft	56

List of Figures

1.1	Typical ring resonator output characteristic (in blue), over which are highlighted all its the notable parameter. The characteristic of the same ring, but with some changes in its constitutive parameter, like for example the refractive index of the cladding	19
1.2	Left: comparison of the absorption spectrum of ammonia (in red) and ammonia+air (in blue). Right: notable absorption peaks of different gaseous compounds with related detectable concentration.	20
1.3	Absorption spectra in the infrared region of some notable chemical compounds important in the biomedical field and air quality control	20
1.4	Measured losses in dB cm^{-1} in the mid-infrared region according to [6]	21
1.5	Power distribution of the first two modes of a rectangular shaped waveguide computed with a FEM in the RSoft CAD software. The waveguide is a 500 nm x 220 nm Si rail in SiO_2 , with a freespace wavelength of 4 μm . Left: the power distribution of the first quasi-TE mode. Right: the power distribution of the first quasi-TM mode.	23
1.6	Power distribution of the first mode of a rectangular shaped waveguide with different heights computed with a FEM in the RSoft CAD software. The waveguide has a fixed width of 500 nm and the simulation is performed with a freespace wavelength of 4 μm . Left: The height is fixed to 220 nm. Center: The height is fixed to 150 nm. Right: The height is fixed to 90 nm.	23
1.7	Power distribution of the first mode of a rectangular shaped waveguide compared to a slot waveguide with a FEM in the RSoft CAD software. The waveguide has a fixed width of 500 nm and the simulation is performed with a freespace wavelength of 4 μm . Left: The power profile of a standard 500 nm x220 nm waveguide . Right: The power profile for a slot waveguide with slot dimension fixed to 100 nm and rails dimension to 200 nm.	24
1.8	Left: illustration of a measuring system composed by two cascaded MRR. To notice how the reference ring is covered by the cladding and the sensing ring is exposed. Right: illustration of the spectra of the reference ring (top), the sensing ring (middle) and the whole system (bottom). In red dashed lines are reported the spectra in case of a refractive index change in the sensing region and it can be appreciated the magnifying effect on the spectrum of the whole system.	24
1.9	Example of surface functionalization for complementary DNA sensing.	25

2.1	Detail of the computed discrete spectral shift as a consequence of different variation of n_{eff} in the two cascaded ring configuration (Vernier effect) [19].	29
2.2	Schematic of the three cascaded ring configuration proposed in [20]. In red and yellow are highlighted the sensing and reference path respectively. . . .	29
2.3	Results coming from the calibration procedure of the device proposed in [22]. Left: time response with different concentration of complementary and non complementary DNA sequences. Right: calibration curve as a function of the DNA segment concentration.	31
2.4	Picture of the MZI-based system proposed in [24]. Of particular interest is the aperture opened over the sensing arm, defining the sensing chamber in which the target analyte can be poured.	31
2.5	Left: A schematic example for the description of the functionalization procedure, with particular emphasis in the buffer steps needed between each measurement. Right: time response of the sensor proposed in [25].	32
2.6	Picture of the device proposed in [25] in which can be noted the VOAs and phase shifters systems, with zoom in the RR region (sensing chamber). . .	32
2.7	Computed improvement in the transmittance exploiting different architectural solutions.[25]	33
2.8	Spectral response of the device proposed in [25] with two different avidin concentrations.	33
2.9	Schematic of the device proposed in [26] for CH ₄ spectroscopy.	34
2.10	Absorption spectra in IR region for CO ₂ , H ₂ O and CH ₄ to justify the choice of the operating frequency. [27]	35
2.11	Left: field distribution for the fundamental quasi-TM mode in the waveguide configuration proposed in [14]. Right: time response of the device as different gaseous mixtures are inserted in the sensing chamber.	35
2.12	Detail of the suspended waveguide structure proposed in [27]. The field distribution for the fundamental mode together with the modal characteristics is shown in the top right inset.	36
2.13	Experimental results reported in [27], computed by the evaluation of the three outputs, demonstrating sensitivity down to 1000 ppm	37
2.14	Two cross-section solutions for ultra-sensitive devices.[28]	37
3.1	Image of the whole device. The laser radiation is first sent to a 1 × 8 splitter; the phase control section is then used to tune individually the phases of the fields in each waveguide; the resulting fields are recombined by a tapered MMI before illuminating the target. The ring resonator placed right after the laser source is used for monitoring.	40
3.2	Illustration of a typical slab waveguide	41
3.3	Dispersion relation of the first five modes of a slab waveguide . The blue dots represent the cut-off frequency for each mode, whereas the black ones are in correspondence of the n_{eff} of the modes when the frequency is fixed. Graph obtained with the MatLab program in A.1	42
3.4	Dispersion relations of the first five modes of a slab waveguide with a slight variation in the cladding refractive index . On the right is possible to see a zoom to better appreciate the shift.	43

3.5	Field distributions of the first mode of a slab waveguide . The red vertical lines represent the edges of the core. It is as a consequence evident how the fields extend their evanescent tails outside the core region in the cladding and in the substrate.	44
3.6	Left: dispersion relations of the fundamental mode of a squared waveguide with different dimensions. Right: dispersion relations of the third mode of a squared waveguide with different dimensions. Please note the flattening of the blue curve (associated to side dimension of 1 μm) at high free-space wavelength, clear sign of a mode below cut-off.	45
3.7	Left: dispersion relations of the fundamental mode of a rectangular waveguide (height fixed to 220 nm) with different widths. Right: dispersion relations of the second mode of a rectangular waveguide (height fixed to 220 nm) with different widths.	45
3.8	Temperature variation ΔT (left) and refractive index variation Δn (right) in a transverse cut as the temperature increase of the metal strip is fixed to 50 $^{\circ}\text{C}$. One can appreciate how the refractive index of the close waveguide is clearly modified, whereas the one of far apart waveguide is slightly touched (remember that in figure the spacing is fixed to 17 μm , when in the final configuration the distance will be 25 μm)	47
3.9	Left: Δn_{eff} of the fundamental mode of the waveguide close to the metal strip. Right: Δn_{eff} of the fundamental mode of the waveguide far from the metal strip. (Please note the different scales)	48
3.10	Power difference in two sub-branches belonging to the same branch normalized to the power at the input port as a function of the $L_{tap,2}$	50
3.11	Schematic of the final 1-to-8 splitter obtained in the RSoft environment	50
3.12	Simulation results for the optimized 1-to-8 splitting structure, in which can be appreciated the good balance between each branch. ("Launch 1, 2, etc" are the normalized power in different branches)	51
3.13	Simulation results for the 1-to-4 splitter exploiting MMIs. This results shows how there is a not perfect balance in the second splitting stage.	52
3.14	Left: BEAMProp simulation results of the 4-to-1 MMI combiner with random input phases. Middle and right: far field distributions obtained with two different set of input phases to demonstrate the beam steering capability of the system.	54
3.15	Top-left: BEAMProp simulation results of the 4-to-1 MMI combiner with tapered width and random input phases. Top-right: far-field distribution obtained with zero relative phase-shift between the branches. The result is a symmetrical, single (narrow) lobe response. Bottom: far-field distributions obtained with random input phase-shift to demonstrate the possibility of obtaining many significant output lobe at different propagation angles.	55
3.16	Schematic of the final 8-to1 MMI tapered combiner obtained in the RSoft environment	56

3.17	Top: far-field distribution obtained with zero relative phase-shift between the branches (left) and with a 30° phase-shift just at IN1. In the former case the result is a symmetrical, three-lobed (narrow) lobe response, whereas in the latter the result is blended. Bottom: far-field distributions obtained with random input phase-shift and with just 15° difference at port IN2 to demonstrate the flexibility of the system and its promising characteristics in terms of single-pixel condensed imaging.	57
3.18	The 1-to-2 nano-structured MMI with programmed presence of silica holes in the central splitting region.	58
3.19	Error convergence obtained with a NN algorithm trained with 70% of the obtained data and tested with the other 30%. The RMSE converges to approximately 17%	60
3.20	Layout mask for the designed OPA device. Red: optical Silicon waveguides; blue: electrical connections. The central thermal-tuning region is 10 times shorter for better readability.	60

Chapter 1

Introduction

1.1 Motivations

In order to start the main dissertation one has to define what a biosensor is, or more in general what a sensor is. A sensor is a self-contained device that is capable of providing real-time analytical information about a test sample [2]. Indeed a sensor is a device able to perform some measurement on a sample (that from now on will be called target species or analyte), through two different mechanisms: recognition and transduction. The recognition process is possible through a more or less selective interaction between the analyte and the recognition element. This interaction will cause somehow a change that can be transformed into a physical alteration by the transducer element, allowing the final measurement.

In certain types of sensors, no physical distinction between the sensing element and the transducer can be made. The transduction mechanism exploited for all the sensors treated in this work is the electromagnetic interaction with the analyte, that's why they fall into the family of optical transduction based devices. In particular optical transduction is achieved by monitoring a physical quantity connected to light propagation through the sensing element: for example the refractive index and the absorption spectrum.

To better appreciate the potential of the family of sensors treated in this work it is useful to enumerate some of the characteristics that are nowadays required from a sensing system in general: smallness that can be strictly related to portability, easiness of parallel fabrication of many devices together and scalability to mass production, low cost, high sensitivity and selectivity to a specific target property. In the following paragraphs it is cleared how many of these features are matched by Silicon-based optical sensors.

1.1.1 Technology

As regard the technology exploited for the fabrication, the realization of photonic sensors takes great advantage from the advance of the Silicon microelectronics industry. Employing this mature technology, which is more than 30 years old, it is possible to manufacture high-density photonic integrated circuits (PIC) by means of the complementary metal oxide semiconductor (CMOS) technology, to the extent that silicon is becoming the material of choice for PIC. This is because the integrated optics technology allows the integration of passive and active optical components (such as waveguides, couplers, filters, detectors and

even sources) onto the same silicon substrate, allowing the flexible development of compact sensing devices. The possibility to fabricate a large amount of chips with a small effort is strictly related to one of the great merit of this kind of sensor: the low cost. Another great merit of such devices is strictly related to their intrinsic nature of being (almost) completely integrated: they can be really small (in the order of a millimeter squared or less). Being so small is also a further reason for the moderate price per device because a large number of them can be put onto the same wafer. Together with the CMOS technology also the microfluidics can find vast exploitation in such a field. Indeed as it will be better clarified in the following chapter the sensing procedure is possible thanks to the creation of a sensing chamber over the silicon substrate in correspondence of a waveguide segment. In order to fill this chamber with the wanted sample can be useful to integrate the optical system together with a microfluidic circuit. This is useful to control the filling operation and avoid dispersion and waste of the analyte.

1.1.2 Applications

A consequence of the smallness of the devices is the portability and the possibility of an easy integration in many different systems. This is one of the main reasons why Silicon-based optical sensors have a great appeal in many different fields, starting from the biomedical one to the control of liquid and gas quality in industry. For example in the agricultural field there is great need of devices able to monitor the emission of harmful gasses, and in farms air must be monitored to ensure the ventilation requirements for the health of the livestock [13]. Furthermore in the biomedical field they can be used to perform non invasive analysis over human liquids or, for example, the human breath [13].

Keeping on the biomedical subject this family of sensor can become an inexpensive alternative to the expensive and multi-functional analytical equipment that are the conventional chemical and microbiological assays. This is valid in general for all the biosensors that have been developed in recent years: try to provide (an alternative and) something that can work in parallel with the tests that are normally done in laboratories, tests that in one hand are reliable and efficient but on the other hand are costly and possibly slow (can require hours or even days to obtain a result due to the pace of biology) [11]. In particular Silicon based optical sensors can find their spot of application together with many other classes of sensors due to increase in the need of fast and simple monitoring of the environment and human health. Their peculiarity with respect to the many other classes of sensors is that they are "label free". Precisely many of the current widespread assays and sensors requires the use of a "label" that is directly present in the analyzed sample and its a marker for the effectiveness of a certain reaction certifying the presence of the target species. This is because very often the compound involved in the recognition process is not easily detectable and one must resort to a trasduction label that is activated proportionally to the characteristics of the sample. The so called "label" is nothing but a co-reagent involved in the recognition process and can be a simple molecular species or a nanoparticle that can be easily detected by the transducer. An example of labels largely used in assays are the fluorescent labels. They are molecules chemically bonded to the functional groups of the target species and they derive from special chemical compound called fluorophores. With such fluorescent labels the properties of the analyte can be defined by monitoring the output signal generated by the labels. The use of label can have a large impact on the

cost of the device and on the time needed for fabrication (because of the introduction of this secondary receptor-transducer mechanism) making their manufacture standardization difficult.

This is not the case for the optical sensors analyzed below because they rely directly on the propagation of light in waveguide and the way propagation is affected by changes in the analyte. That is why there is so much interest in the development of this new class of devices: they can be really cheap and simple. Moreover labeling not only increases the time and cost of an assay but also can also alter binding interactions and it insert a new source of errors. On the other hand the lack of labels makes the interaction between sample and sensor less specific, that is why an extensive characterization of the analyte is needed before the possibility to have a sensor analyzing it. Moreover in order to increase the selectivity, that is the ability to distinguish between a specific target species and any other substance and producing as a consequence an output signal strictly related to its presence, it is proposed to functionalize the transducer surface [3]. This procedure is particularly diffused whenever the target species is dispersed at low concentration in a solution together with other substances. It consists in exploiting specific bonding interactions, such as the antigen-antibody one, in an adlayer over the waveguide .

1.1.3 Characteristic of a biosensor: figures of merit

To further investigate the way an electrical field interactions with the sensor it is convenient to give the definition of the figures of merit describing such an interaction. Indeed all this definitions are coming in handy in chapter 2.

The first figure of merit has been already introduced in the previous section and it is the *selectivity*, i.e. the capability of a sensor to detect a target analyte in a sample containing other admixtures. Other two very important FOM are the *detection limit* (DL) and the *sensitivity*. The former is defined as the lowest quantity of concentration of the analyte that can be distinguished with a certain degree of confidence from the absence of it. Generally a good DL value (i.e. a low value) is obtained when the background noise is sufficiently low. The latter is defined as the change in the response quantity as a consequence of an unitary change in the analyte. For example in the family of sensors relying on the refractive index change, the sensitivity is given in refractive index unit (RIU). Moreover it is possible to define the *response range* as the range in which the measurement are provided with a given level of confidence. The lower limit is clearly fixed by the DL, whereas the upper one can be determined by a marked deviation with respect to the calibration curve. Finally it is useful to define the resolution, namely the smallest detectable change in the analyte concentration [2].

1.2 Basic principles

As previously mentioned the devices treated in this work belong to the family of optical sensors based on Silicon technology, however a distinction in two different families has to be made. The first family operations are based on the possibility to measure a change in the refractive index of the target sample caused by some variation in the analyte itself; the second one relies on the change in the absorption spectrum of the target sample. The basic

building block for every sensor is the waveguide and the fact that the evanescent tails of the field propagating into a waveguide come into contact with the sample under test; according for example to the concentration of a specific compound in the sample the refractive index in a region close to the core of the waveguide is changed and as a consequence the shape of the modes of propagation is changed as well as all the other modal properties (see 3.2). That is why this method of sensing is commonly defined as "evanescent field detection principle". Another method exploited in optical sensor can be called for simplicity "direct interaction". It means that the light, that can be generated inside or outside the device, interacts directly with the analyte and what is measured is the reflected or transmitted signal. The direct interaction can be obtained by generating a chamber into the device in which the analyte can be poured or by investigating sample outside the chip. This is the context in which the device treated in chapter 3 operates.

1.2.1 Refractive index variation

This section presents the basic concepts related to the measurement of a change in the refractive index . This variation is generally investigated using interferometric or filtering systems. In particular in this type of architectures the basic building blocks can be a Mach-Zehnder Interferometer (MZI) or a ring resonator (RR). The basic idea wherever a MZI-like architecture is adopted is to create a sensing chamber over one of the two branches (sensing branch) by etching the cladding, in order to allow a direct contact between analyte and waveguide . As it is pointed out in 3.2, the change in the refractive index of the analyte will change the propagation characteristics of the modes inside the sensing arm and as a consequence the effective length of this branch, producing the classic interferometric pattern at the output. The optical intensity at the output is proportional to the cosine of the difference of the phase-shifts in the two branches. The phase-shift difference $\delta\phi$ can be written as:

$$\delta\phi = k_0 L_s (n_{eff,s} - n_{eff,r})$$

where k_0 is the propagation constant in free-space, L_s is the length of the part of the sensing branch inside the sensing chamber, $n_{eff,s}$ and $n_{eff,r}$ are the effective refractive index of the signal propagating in the sensing and in the reference arm respectively. From the output intensity, together with the previous characterization of the sample, one could extract the quantities of interest. Generally the variation of the $n_{eff,s}$ as a consequence of the variation of the target species concentration, is very low, that is why there is the need for very high L_s (in the order of cm) in order to increase the sensitivity.

A similar idea is exploited by the architectures based on ring resonators. The sensing chamber is generally drilled over the ring in order to vary the resonant properties of the ring itself. Indeed the resonant wavelengths of a closed circular waveguide are defined as:

$$\lambda_{res} = L_r n_{eff} / m, \quad m = 1, 2, 3, \dots,$$

where L_r is the length of the ring and n_{eff} is the effective refractive index of the wave travelling in the ring. Clearly a variation in the sample causing a variation in n_{eff} can be detected as a variation in the spectral characteristic of the ring as can be qualitatively seen in figure 1.1, where two other characteristics of RR are highlighted, namely the Free Spectral Range (FSR) and the Full Width at Half Maximum (FWHM). The FSR is the

distance in wavelength (or frequency) between two resonant peaks, the FWHM is the width in wavelength (or frequency) between the -3dB points of the same resonant peak. From these two definitions one can define the Quality (Q) factor of the ring itself:

$$Q = \frac{\lambda_{res,0}}{FWHM},$$

where $\lambda_{res,0}$ is the resonant frequency. The Q is strictly related to the number of revolution that a signal inside the ring experiences before exiting from it, that is directly related to the sensitivity of the devices. The interaction length in a ring having a large Q-factor will be high and as a consequence the sensitivity of the device. The Q factor can be enhanced by lowering its losses and as a consequence lowering the capability of coupling it with the external world, a trade-off has to be made.

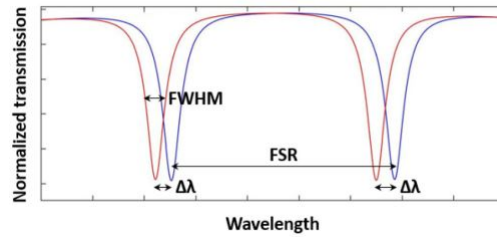


Figure 1.1: Typical ring resonator output characteristic (in blue), over which are highlighted all its the notable parameter. The characteristic of the same ring, but with some changes in its constitutive parameter, like for example the refractive index of the cladding, is reported in red.

In general a ring solution is preferable because of its compactness, meanwhile a MZI solution is demonstrated having higher sensitivity also due to its higher size.

1.2.2 Absorption spectroscopy

Alternatively to a variation in the refractive index, absorption spectroscopy can be at the base of another family of sensors. In contrast with the refractive index sensing that is generally exploiting the mature telecommunication technology at $1.55\ \mu\text{m}$, the spectroscopy bases its functioning over a wider frequency range. The short-wavelength infrared (SWIR, $1.4\ \mu\text{m} - 3\ \mu\text{m}$) and mid-wavelength infrared (MIR, $3\ \mu\text{m} - 8\ \mu\text{m}$) are region of the electromagnetic spectrum that are of great interest for biosensors, since in this ranges are contained strong vibrational signatures for a number of gases and molecules[7].

It is reported [15] that many different gaseous compounds of interest in environmental and agricultural monitoring have significant absorption peaks in the C and S telecom bands (see figure 1.2). The MIR region is for sure the region of greatest interest for the biomedical applications. Indeed many absorption peaks of molecule such H_2O , CO_2 , $C_6H_{12}O_6$ can be found in this region as can be seen in figure 1.3. The infrared spectroscopy exploits these peaks to sense the presence of a specific molecule and of specific bonds, since each peak is related to a specific vibrational or rotational mode of the molecule itself; moreover the

intensity of the peak can be related to the concentration of the target analyte.

A key requirement that an optical device must fulfill is the low power loss, strictly related

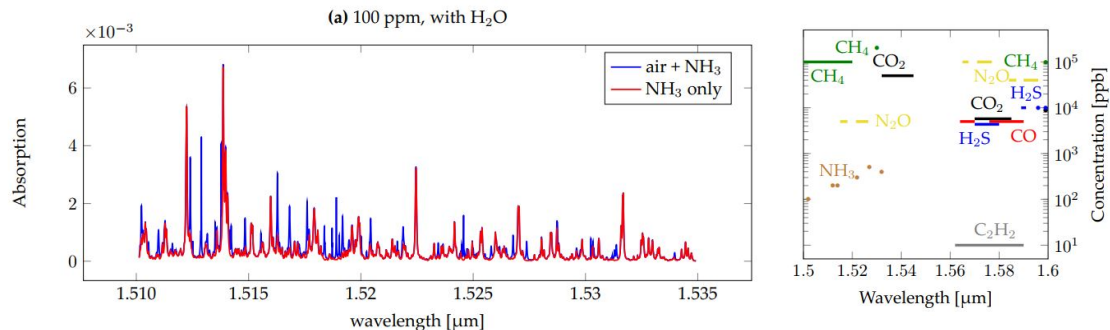


Figure 1.2: **Left:** comparison of the absorption spectrum of ammonia (in red) and ammonia+air (in blue). **Right:** notable absorption peaks of different gaseous compounds with related detectable concentration.

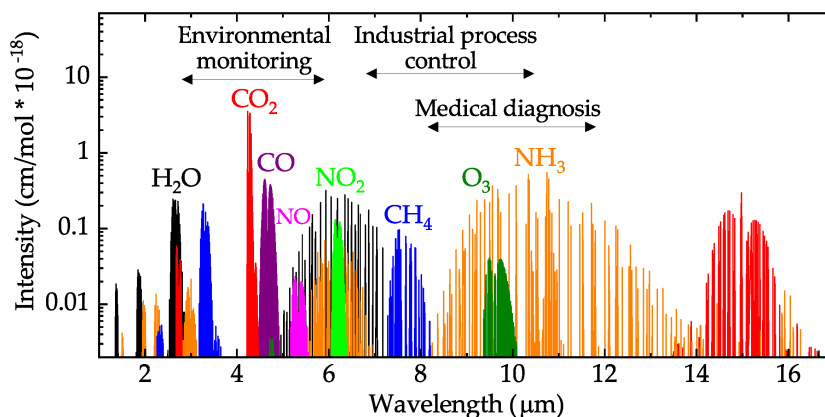


Figure 1.3: Absorption spectra in the infrared region of some notable chemical compounds important in the biomedical field and air quality control

to the low power consumption. A further consideration is that the most widely used material in PIC (Silicon) is transparent just up to 8 μm. Similarly Germanium, that is another material used as guiding material in PIC, is transparent only in the range 2 μm – 14 μm. This is clearly limiting the range of application of these two materials. Moreover the Silicon-on-insulator (SOI) technological platform can only be used up to 4 μm due to the high losses of the Silicon dioxide. In figure 1.4 the propagation losses of the SiO₂ are reported vs. frequency. As a consequence in recent years many other technological platforms has been investigated to expand the possible range of application of Si in PIC. Some example are the Silicon-on-Sapphire (SOS) and the Silicon-on-Silicon Nitride (SON). SOS and SON exploits as cladding material Al₂O₃ (transparent up to 5 μm) and Si₃N₄ (transparent up to 6.5 μm) respectively. From the technological point of view a SON wafer can be obtained by bonding a Si wafer to a Si₃N₄ one and by etching back the Si in excess.

A further approach to increase the working range is to remove the cladding material replacing it with air (that is transparent up to $8.5\ \mu\text{m}$), creating as a consequence suspended structures (figure 2.12). This can be done by adding some supplemental feature in the design flow in order to be able to undercut the waveguide preserving its guiding and mechanical properties [5]. Another technological platform having wide application in PIC is the Si/SiGe/Ge one. Guiding structures made by SiGe can be grown over a Si wafer and can work up to $8\ \mu\text{m}$ [8]. In order to extend the working region, Ge waveguide cladded by thick layers of SiGe can be used.

Finally waveguides with larger dimensions are often used in Infrared spectroscopy to fully

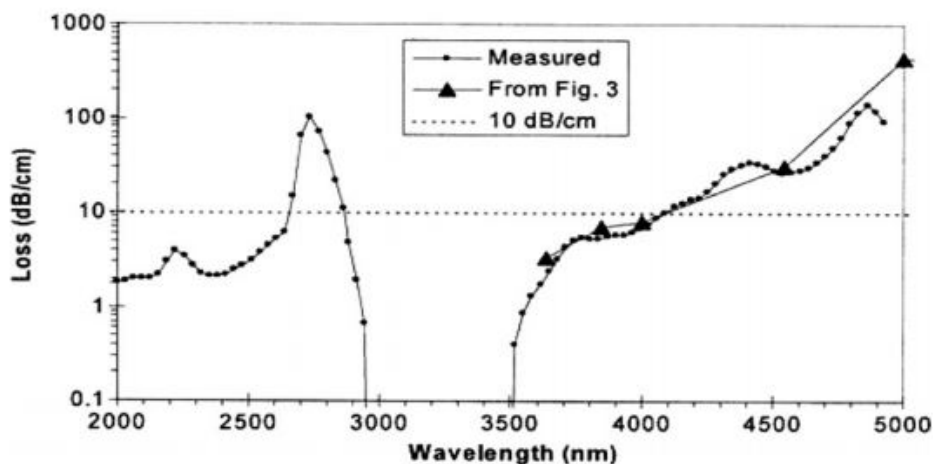


Figure 1.4: Measured losses in dB cm^{-1} in the mid-infrared region according to [6]

exploit the transparency range of the materials. This is done to increase the CF (see 3.2) of the guided field in order to lower the losses. For example in the SOI platform are largely diffused thicker overlayers than the common 220 nm exploited in integrated systems. Indeed 400 nm and 500 nm overlayers are quite common, where the CF of the fundamental mode is quite high and structures like interferometers and couplers can be designed to work up to $4\ \mu\text{m}$. Clearly this solution is relevant for all the applications not relying on 'evanescent field sensing' where the CF is required to be low, but in all the application where the sample under test is outside the chip. This situation is largely diffused in the so-called imaging sensor family. In this type of application the goal is to recreate an image of the target by scanning it with a focused beam of light. To do that are largely diffused Optical Phase Array structures, thanks to which it is possible to implement an integrated beam steering architecture.

Optical phase array for beam steering applications

At this point it is interesting to report some basics concerning OPA architectures. They find natural application in the communication field, especially in space [34], but are nowadays studied also for biosensor applications [29][30]. In general they can be useful in a device in which it is necessary to control the emitted far-field distribution in order to reconstruct images. This is the context in which the device treated in section 3 fall.

An OPA is generally constituted by: an optical coupler, an optical power division network, some phase-shifters and an optical antenna. The basic idea is to divide the input signal in a sufficiently high number of sub-branches in which the relative phase is controlled by the phase-shifters. Then the signals can be re-combined in a single waveguide segment and radiated through a grating antenna or combined in a more complex multi-dimensional antenna array to achieve better far-field tunability in terms of steering range and beam-width. The phase tuning system can be implemented exploiting electro-optic effects achieving good results in terms of modulation band-width together with bad results in terms of efficiency. On the other hand can be used the thermo-optic effect, obtained through a heater (metal wire) near the waveguide. This solution is particularly good in Silicon Photonics because of the high thermo-optic coefficient of silicon and to the fact that do not increase the losses (the imaginary part of the refractive index is not modified) except for the absorption ones related to the vicinity of the metal wire to the waveguide.

From the first totally integrated OPA solution in 2009 characterized by a very limited steering range (2.3°) and beam-width, research has come a long way. In recent years are reported OPA achieving more than 30° of steering range with a beam-width lower than 1° [34].

1.2.3 How to improve the architectures

Back on 'evanescent field sensing' in this section are reported some solutions to improve the sensitivity of the architectures. All the solutions have the objective to lower the CF in order to increase the penetration length of the evanescent field surrounding the waveguide. A first solution that can be easily implemented by choosing the right source element is to use sensing field that are quasi-TM polarized. In section 3.2 it is evident how a quasi-TM field has a lower CF at fixed frequency with respect to the quasi-TE one. In figure 1.5 can be seen the field distribution of the first two modes of a rectangular section waveguide. As a consequence it is demonstrated how such solution can improve the sensitivity of the sensor [10]. Another solution going in the same direction is to use thinner waveguide than the normally used. Indeed by lowering the height of the waveguide the same mode at the same frequency will be less confined (see figure 1.6). This is why in the sensor field it is common to the 90 nm or 150 nm waveguide instead of the standard 220 nm one.

A different waveguide approach is the one concerning SOI slot waveguide, consisting in two parallel rails separated by a small gap. This geometrical solution leads to two effects: light is partially confined in the gap and the intensity of the field can be extremely high. Indeed the portion of the field outside the guiding rails (in the gap and in the outside cladding) can be higher than 70%, that compared to the CF of the standard rectangular waveguide (at most around 30%) it is significantly higher. This geometry can be obtained by standard CMOS processes, that can be the key for a possible wide use in future applications. The reason for the high confinement in the slot is the refractive index contrast between the cladding and the core. Higher the contrast, higher will be the intensity of the field in the slot region, because higher will be the discontinuity encountered by the normal component of the electric field. The field enhancement in the low index region can be written as:

$$E_{norm,slot} = \frac{n_{core}^2}{n_{slot}^2} E_{norm,core},$$

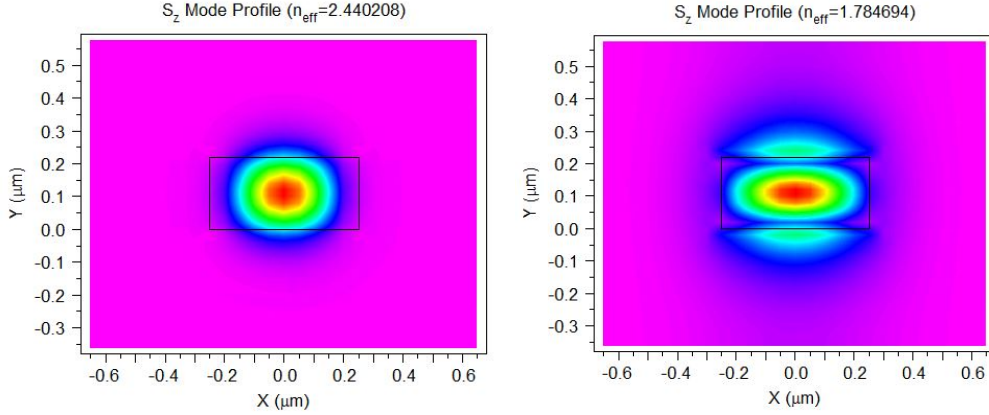


Figure 1.5: Power distribution of the first two modes of a rectangular shaped waveguide computed with a FEM in the RSoft CAD software. The waveguide is a 500 nm x 220 nm Si rail in SiO_2 , with a freespace wavelength of 4 μm . **Left:** the power distribution of the first quasi-TE mode. **Right:** the power distribution of the first quasi-TM mode.

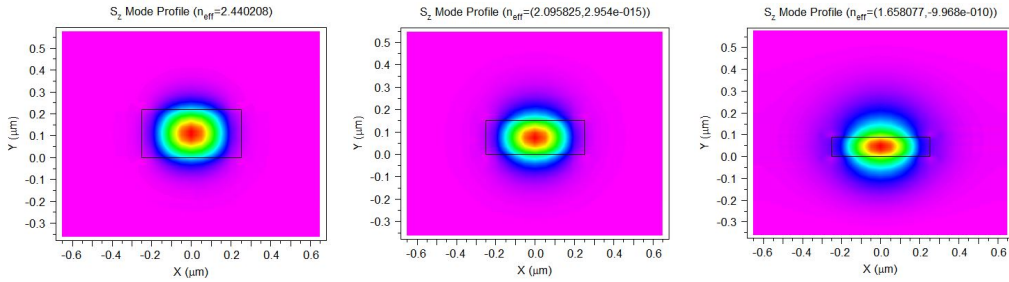


Figure 1.6: Power distribution of the first mode of a rectangular shaped waveguide with different heights computed with a FEM in the RSoft CAD software. The waveguide has a fixed width of 500 nm and the simulation is performed with a freespace wavelength of 4 μm . **Left:** The height is fixed to 220 nm. **Center:** The height is fixed to 150 nm. **Right:** The height is fixed to 90 nm.

that for example in the case of Si core and SiO_2 at around 1.55 μm is around 12.

The slot platform finds wide use in the sensing field as in literature one can find devices based on MZI with slotted waveguide in the sensing arm together with slotted MRR. It is reported [9] that slotted MRR can achieve sensitivity more than three times higher with respect to the conventional strip waveguide based MRR. This is due to the fact that the shift in frequency due to the change in the resonant frequency is directly proportional to a change in the n_{eff} , being directly proportional to the CF.

Finally a solution often exploited in the systems based on MRR is to cascade two or more MRR with different FSR, in order to take advantage of the Vernier effect. For example in a system cascading two rings (see figure 1.8) only one of the two will have the upper cladding removed, being the actual sensing ring. The spectral response of such a structure will present some major peaks together with some minor ones, thanks to the difference in FSR of the two rings. The difference in FSR of the rings will determine the distance of

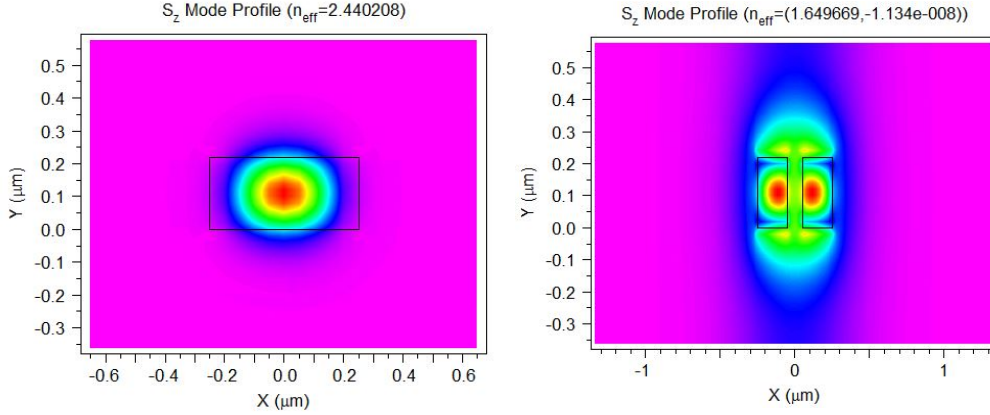


Figure 1.7: Power distribution of the first mode of a rectangular shaped waveguide compared to a slot waveguide with a FEM in the RSoft CAD software. The waveguide has a fixed width of 500 nm and the simulation is performed with a freespace wavelength of 4 μm. **Left:** The power profile of a standard 500 nm x 220 nm waveguide. **Right:** The power profile for a slot waveguide with slot dimension fixed to 100 nm and rails dimension to 200 nm.

the major peaks of the whole system, being larger as the difference in FSR is smaller. If the refractive index over the sensing arm changes, it will cause a shift in the spectrum of the sensing ring, that will have an amplified effect on the system spectral response, amplifying as a consequence the sensitivity of the device. In figure 1.8 this effect can be seen qualitatively. The amplifying coefficient will be higher as the difference in FSR is lower, causing a sensitivity magnification of even more than one order of magnitude [10].

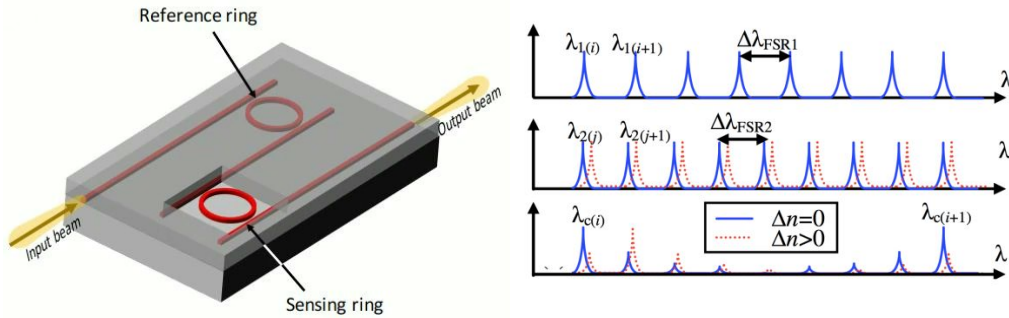


Figure 1.8: **Left:** illustration of a measuring system composed by two cascaded MRR. To notice how the reference ring is covered by the cladding and the sensing ring is exposed. **Right:** illustration of the spectra of the reference ring (top), the sensing ring (middle) and the whole system (bottom). In red dashed lines are reported the spectra in case of a refractive index change in the sensing region and it can be appreciated the magnifying effect on the spectrum of the whole system.

1.2.4 Functionalization of the surface

In section 3.2 it is explained why the characteristics of a waveguide are particularly sensible to variation close to the waveguide itself. In this section it is made clear how the functionalization of the surface is a key aspect in the preparation of a sensor. Functionalization means immobilization of a biochemical element to the surface of the device in order to ensure efficient and specific interaction with the target species [4]. The choice of the biochemical element is dependent on the specific application, taking into account the requirement concerning sensitivity and stability over time.

The functionalization can be realized by means of physical electrostatic or hydrophobic interaction by simple deposition over the sensing surface. This solution is the easiest from a technological point of view but suffers from the problem of desorption.

Another approach relies on the chemical covalent bonding of the receptor species to the target surface. In order to make possible the chemical bonding the surface of the waveguide needs to be previously activated. In the case of Si and other Si-based materials is largely used the Silane (SiH_4) chemistry: the hydroxyl groups generally exposed at the Si surface can be converted into oxane bonds between the Si and organic compounds by means of intermediate reaction with SiH_4 . Another key step is the choice of the receptor agent, that needs to maintain its performance as a receptor even after the bonding with the waveguide. For example for blocking nucleic acid sequences are largely used as receptors complementary DNA segments (see figure 1.9), whereas to block proteins are used molecules exhibiting thiol ($-SH$) or carboxylic ($-COOH$) groups. In the next chapter are presented some other examples of functionalization of waveguide surfaces, relying even on non-covalent bonding (see the left image in figure 2.5).

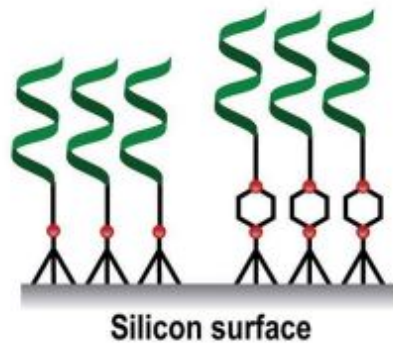


Figure 1.9: Example of surface functionalization for complementary DNA sensing.

Chapter 2

State of the art of Silicon based biosensors

This second part of the thesis is a review of some of the many devices proposed in literature in the last years. The goal is to highlight the aspect introduced in the previous chapter, by going through different types of architectures and technologies that can be found in the label-free integrated photonic biosensors field. Furthermore reviewing different types of sensor allows for comparisons between different solutions concerning the main figure of merit already introduced. The first chapter concerns devices basing their functioning on RI variation, whereas the second one reviews sensors relying on evanescent field absorption spectroscopy.

2.1 Sensors based on refractive index variations

2.1.1 MRR solutions

The first class of devices that I encountered is the one based on resonators. Starting from basic architectures including only one ring resonator, in literature can be found more complex architectures exploiting more rings, in order to solve some of the problems of the basic single-ring ones.

For example in [16] it is presented the idea of a research group of the University of Missouri-Kansas City of a sensor for breast cancer detection. The system is composed by a waveguide and a ring resonator, whose cross-sectional dimensions are the standard 500 nm x 220 nm. The source is a multi-wavelength laser (with center frequency at 1.55 μm) external to the chip that needs to be coupled through optical fibers and surface grating couplers; the photodetector is outside the sensing chip as well and it needs a similar coupling structure. For the couplers the idea is to use already designed and standardized couplers, optimized for 1.55 μm . This device is thought in a multi-sensor platform in which parallel detection of different analytes can be performed concurrently simply by having functionalized different rings (in different chambers) with different antibodies. In particular this sensor will be functionalized with the antibody associated with the Cancer Antigen 15-3 (CA15-3), that is a biomarker useful in diagnosis and in the subsequent monitoring phases of a breast

cancer. This is possible because the antigen-antibody interaction varies the refractive index of the solution in which are present. In many different papers it is in particular reported how the refractive is dependant on the concentration of the CA15-3 over a wide range of wavelength.

In [17] it is demonstrated the use of micro-ring resonators to perform parallel detection of five different clinically relevant protein biomarkers, namely carcinoembryonic antigen, prostate specific antigen, R-fetoprotein, interleukin-8 and tumor necrosis factor-R. This specif chip is composed by 20 label-free immunoassays (four for each protein) that can be run in parallel thanks to a PDMS microfluidic device.

As already exposed, a method to improve the sensitivity of ring architectures is to exploit the so called Vernier effect. Such an architecture is for example proposed in [19] where two rings having different FSR are arranged in a cascaded configuration. The output response of the system is characterized by major peaks interleaved by some minor peaks, whose number and distance is related to the FSR mismatch. In particular the device proposed in [19] is composed by two cascaded rings with different radii: R1 (the reference one) is lower than R2 (the sensing one) resulting in $FSR1 > FSR2$ (in wavelength terms). In figure 1.8 is reported a qualitative illustration of the global response of the system. It can be appreciated that when the characteristic of the sensing ring shifts due to a variation in the sensing chamber the major peaks shifts discretely and this shift is equal to multiple of the FSR of the reference ring. The sensitivity of the device is defined as:

$$S = \frac{\Delta\lambda_{FSR1}}{\Delta n_{eff0}} = \frac{\lambda_{1,i}}{n_{eff}} \frac{\Delta\lambda_{FSR1}}{\Delta\lambda_{FSR1} - \Delta\lambda_{FSR2}} = S_0 M \quad (2.1)$$

where S_0 is the sensitivity of the single ring and M is a magnification factor related to the difference in FSR of the rings. This difference fixes also the detection limit of the sensor because fixes the FSR of the system (the two rings together):

$$\Delta\lambda_{FSR,system} = (M - 1)\Delta\lambda_{FSR1}, \quad (2.2)$$

as a consequence the measuring range will be $\Delta n_{max} = \Delta\lambda_{FSR,system}/S$. A rule of thumb in the choice in the FSR in order to have always an output that can be measured is to choose a difference in FSR at most equal to the -3 dB.

Concerning the technological choices, the proposed solution is a $2\ \mu\text{m}$ SOI with $220\ \text{nm}$ overlayer. The two rings bending radius is chosen to be $38.7475\ \mu\text{m}$ and $39.2728\ \mu\text{m}$ (being the 300th and 312th modes at $1.55\ \mu\text{m}$) in order to minimize the bending losses. With such a choice the separation between two subsequent peaks in the output response is $\Delta\lambda = 2.33\ \text{nm}$. By changing the n_{eff} over R2 it is calculated that with a variation of 8×10^{-5} RIU the major peak shifts discretely by one position (see figure 2.1), resulting in a sensitivity of $5886\ \text{nm}/\text{RIU}$, which is at least one order of magnitude higher than the one obtained with the basic one ring configuration.

Together with the sensitivity magnification also the LOD is improved once the system is provided with a sensible enough detector. The measurable range on the other hand remains the same. A solution that can be implemented to increase the measurable range while keeping the sensitivity benefits of the two-rings configuration is to implement a system with three rings. the system is arranged as shown in figure 2.2. R2 and R3 are exposed to the target analyte in the sensing window, while R1 remains covered with the

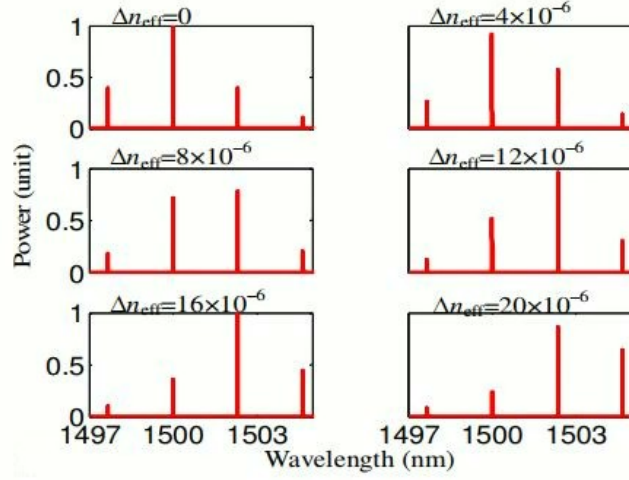


Figure 2.1: Detail of the computed discrete spectral shift as a consequence of different variation of n_{eff} in the two cascaded ring configuration (Vernier effect) [19].

standard cladding. R1 and R2 are cascaded in the same configuration as the previous one, but in parallel it is implemented another measuring channel made by R2 and R3. In such a way we have an enhancement of the sensitivity as in equation (2.1) together with a magnification (M_2) in the measurable range equal to :

$$M_2 = \frac{\Delta\lambda_{FSR3}}{\Delta\lambda_{FSR3} - \Delta\lambda_{FSR2}}, \quad (2.3)$$

the complete demonstration can be found in [20].

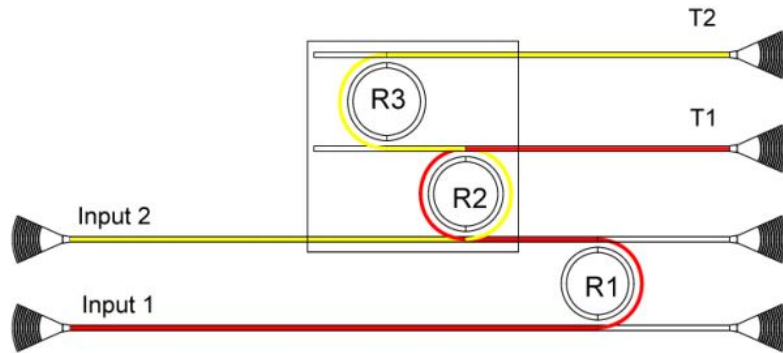


Figure 2.2: Schematic of the three cascaded ring configuration proposed in [20]. In red and yellow are highlighted the sensing and reference path respectively.

2.1.2 MZI solutions

Talking about LOD and sensitivity gives the possibility to introduce the family of devices showing the best results for these two FOM: integrated interferometers. Indeed the system based on ring resonators can show a LOD in the order of 10^{-4} - 10^{-5} [10][20], while are reported interferometric setups showing LOD down to 10^{-8} - 10^{-9} . Such performances can be achieved in systems having very large interaction region, namely very long sensing arm. This is the reason why an interferometric solution is not well suited for systems that need to perform multiple parallel measurements due to the huge size compared to the one exploiting ring resonators (the needed area can be up to 1000 times higher). However it is still the choice for application aiming to highest sensitivity.

A first example of MZI sensor can be found in [21]. The system is a lab-on-a-chip integrating: the actual MZI fabricated with standard silicon technology, a polymer microfluidic delivery system, two diffractive grating coupler for the in-coupling and out-coupling of the light, a photodetector, electronics and software control. The guiding material is a 200 nm wide Si_3N_4 cladded by SiO_2 . The couplers are custom designed to allow efficient coupling in the visible range (being the working range of the system) and their geometry can be defined through electron beam lithography. This simple device was tested for concentration evaluation of HCl and some hormones, showing sensitivities of 1.1×10^{-7} RIU and 1 pM respectively.

Another interesting example of interferometric device can be the one presented in [23], thought for the direct detection of DNA hybridization and for the detection of single mutations at the BRCA-1 gene, involved in breast cancer development. Here it is used a rib waveguide having a 4 nm x 4 μ m rib in Si_3N_4 with 75 nm height core, cladded by SiO_2 . The dimension are fixed to ensure single mode behaviour at the working frequency of 632 nm (an $HeNe$ laser is used as external end-fire coupled source). In order to be sensitive to its target molecule the waveguide in the sensing region must undergo to a series of treatment:

- surface cleaning with a solution of nitric acid and water;
- functionalization with a thiol group exposure through silane immersion;
- attachment of a single-stranded DNA segment (the probe) by covalent bonding to the thiol group.

Measurements are performed by flushing inside the chamber solutions containing complementary or non-complementary single-stranded DNA sequences. It is important to perform a regeneration step after each test in order to ensure complete dehybridization by flowing deionized water with HCl . As reported in figure 2.3, the lowest measurable concentration of complementary DNA segments is found to be 10 pM, whereas any concentration of non-complementary DNA segments results in a not significant measurement. Another remark is that the hybridization with a DNA target with two mismatching bases (corresponding to a mutation of the BRCA-1 gene) can be detected. finally the system is thought to operate together with an integrated microfluidic circuit for solution delivery. This is obtained by two SU-8 photopatterned wafers thermally bonded together and than bonded to the Si wafer.

Another noteworthy solution is the one presented in [24]. In this article it is reported the design and testing of a sensor based on a slotted silicon nitride MZI. Its performances

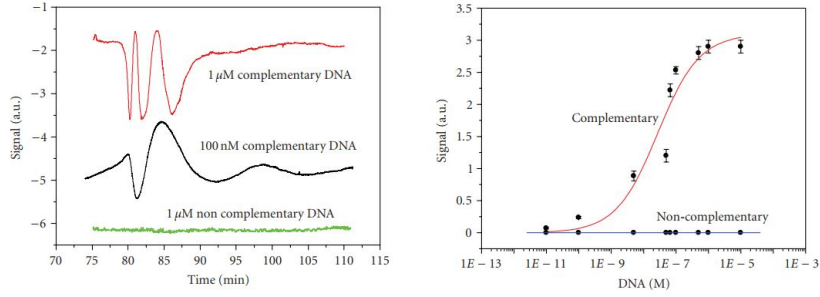


Figure 2.3: Results coming from the calibration procedure of the device proposed in [22]. **Left:** time response with different concentration of complementary and non complementary DNA sequences. **Right:** calibration curve as a function of the DNA segment concentration.

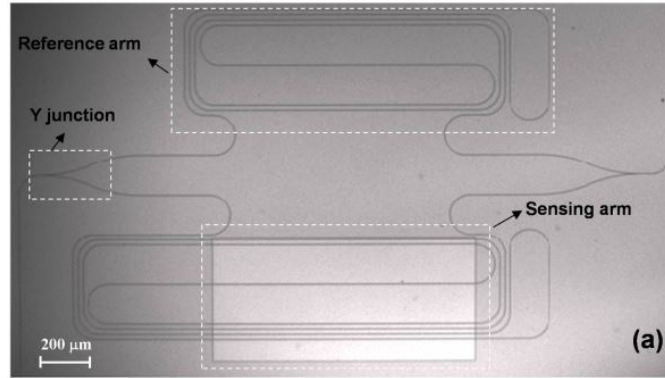


Figure 2.4: Picture of the MZI-based system proposed in [24]. Of particular interest is the aperture opened over the sensing arm, defining the sensing chamber in which the target analyte can be poured.

were tested for the bulk-non-specific concentration measurement of $NaCl$ solution and the specific biotin–streptavidin binding evaluation. An image of the sensor obtained through optical microscopy is reported in figure 2.4. The sensor is composed by an external source (a tunable laser around 1560 nm), vertical couplers to pair the chip to the external world, y-junctions and two many times folded arms in order to increase their length at the same amount of occupied area. The waveguide used is a normal rib waveguide with 75 nm thick rib and 400 nm x 1 μm strip in the reference arm, whereas 400 nm x 1.2 μm strip with a 200 nm slot in the sensing arm. Simulation results show how a variation in the refractive index of the cladding from 1.318 to 1.369 cause a variation in the n_{eff} of 4.06×10^{-4} and 1.59×10^{-4} in the slot and in the strip waveguide respectively, demonstrating the higher sensitivity of the slotted solution. Moreover are reported experimental results concerning the measurement of $NaCl$ concentration, showing a sensitivity of 1.7×10^{-4} RIU that is a better results than the one obtained with strip solution with the same sensing length. Finally it is reported the study regarding the detection of a specific binding: the biotin–streptavidin one, being one of the strongest non-covalent interaction. To do that the surface of the slotted sensing waveguide was treated in order to be functionalized with biotin (an

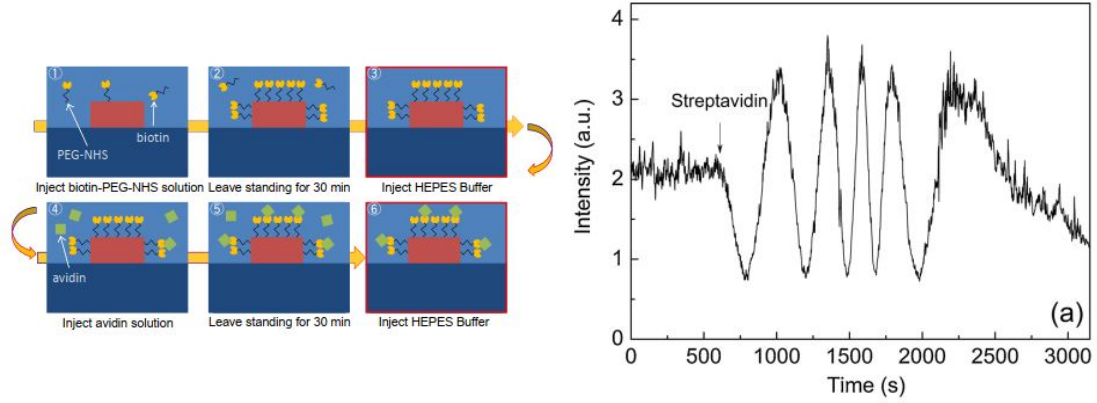


Figure 2.5: **Left:** A schematic example for the description of the functionalization procedure, with particular emphasis in the buffer steps needed between each measurement. **Right:** time response of the sensor proposed in [25].

illustration concerning a similar process can be found in figure 2.5), than streptavidin solution with different concentration can be flown in the sensing area. A real time response to the injection of a $5 \mu\text{g mL}^{-1}$ (namely 95 nM) can be seen in figure 2.5). The LOD is found to be approximately 20 fm .

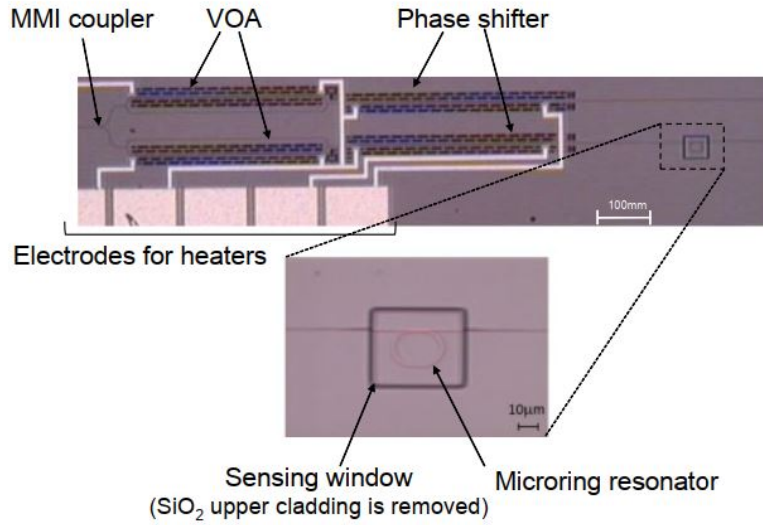


Figure 2.6: Picture of the device proposed in [25] in which can be noted the VOAs and phase shifters systems, with zoom in the RR region (sensing chamber).

A similar specific interaction (the one between biotin and avidin) is investigated with a different architectural solution by [25]. This sensor bases its functioning on a MRR-enhanced MZI, namely on the sensing branch of a MZI there is a MRR in charge of enhancing the phase shift in the branch, resulting in higher sensitivity. The waveguide technology used

is a $210 \text{ nm} \times 400 \text{ nm}$ Si wire cladded by SiO_2 everywhere except the sensing region that is restricted to the MRR area. The splitter and combiners are realized by MMI devices, moreover in both the branches is present a thermally controlled variable optical attenuators (VOAs) in order to obtain higher extinction ratio by balancing the power in each branch. An image of the sensor can be found in figure 2.6. In this article the improvement in terms of amplitudes of the resonant peaks with different MRR solutions is analytically calculated and I report in figure 2.7 the results, together with the same data with different coupling coefficient (K) between the MRR and the coupled waveguide. It is evident how by lowering the K the change is larger, this is because of the greater Q-factor that is proportional to the number of revolution performed by a signal inside the ring before exiting. In order to investigate the protein (avidin) detection capability of the system, the sensing region must be functionalized as in figure 2.5. The device was tested for 200 pM and 20 pM avidin solutions and the results are reported in figure 2.8. Here can be appreciated the shifts in the resonant peaks due the biotin-avidin interaction.

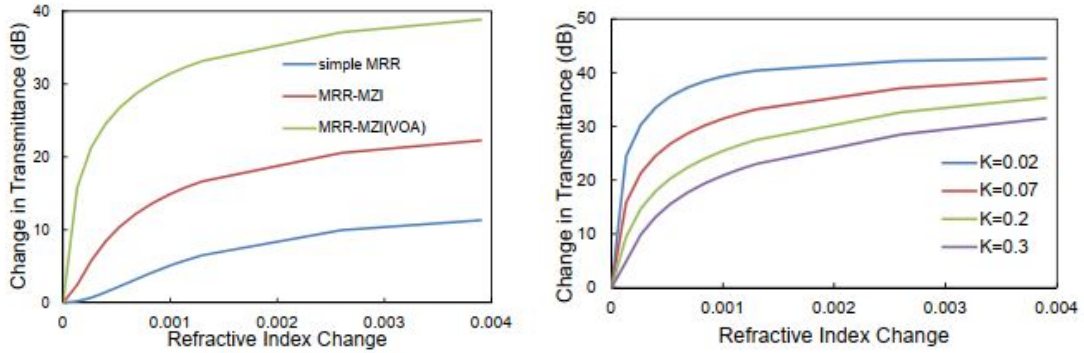


Figure 2.7: Computed improvement in the transmittance exploiting different architectural solutions.[25]

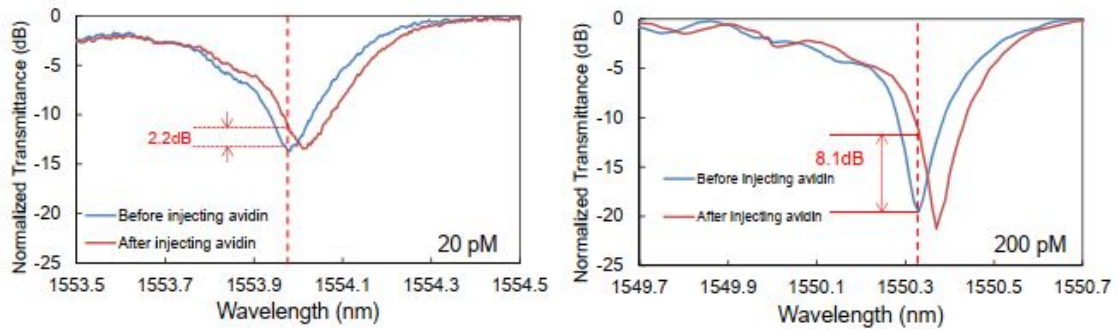


Figure 2.8: Spectral response of the device proposed in [25] with two different avidin concentrations.

2.2 Spectroscopy

In this section the subject is moved to the Silicon photonic devices based on absorption spectroscopy.

The first notable device that can be interesting to analyze is the one reported in [26]. It is a fully integrated on-chip Silicon photonic waveguide absorption spectrometer (SPWAS) for the detection of CH_4 working in the telecommunications U-band (1650 nm). The device exploits a tunable III/V DFB-laser as source and an InGaAs detector that can be integrated with the Si wafer in which it is defined the sensing region. The SPWAS sensor consists of a 10 cm long Silicon waveguide, defined in the Si layer of a SOI chip by standard deep-UV photolithography. An illustration of the SPWAS can be seen in figure 2.9, where it is possible to appreciate that the waveguide is folded in order to occupy an area of just 16 mm^2 . Based on numerical simulations the dimensions of the waveguide are chosen to

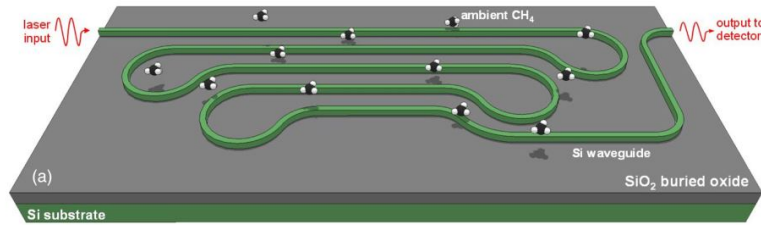


Figure 2.9: Schematic of the device proposed in [26] for CH_4 spectroscopy.

be $430 \text{ nm} \times 250 \text{ nm}$ in order to obtain the first guided TM mode with $n_{\text{eff}}=1.66$ and with $CF=28.3$. These dimensions are chosen to have a sufficient confidence margin over the manufacturing errors (remember $n_{\text{SiO}_2}=1.44$). The cladding over the waveguide is removed and filled with the sample air in the measuring process. The confinement factor fixes the sensing volume of the SPWAS to $8000 \mu\text{m}^3$ (considering as 'sensed' volume the space where the field intensity is higher than $1/e$), resulting in a sensitivity lower than 100 ppm . This result together with the size, cost and power benefits of the CMOS technology explains how devices like this can be an alternative to the nowadays used non-selective chemical sensors or the quite costly and bulky mass spectrometry systems.

Other two interesting applications are the one reported in [14] [27]. These papers treat two different technological solutions for the design of a sensor able to detect CO_2 . Detecting this molecule can be useful both in indoors applications since high levels of CO_2 can affect the human cognitive functions and in outdoors applications due to its well-known climate affections. Both the solutions rely on a specific strong absorption peak (namely the peaks related to the fundamental asymmetric stretching band) in the CO_2 spectrum at $4.26 \mu\text{m}$ that do not overlap with peaks of other gasses widely present in air (such as water vapour, see 2.10). Both the solutions are based on Silicon waveguide but with some peculiarities with respect to the standard SOI solution because, as already mentioned in section 1.2.2, SiO_2 is highly absorbing beside $4 \mu\text{m}$ (see figure 1.4).

The solution proposed in [14] is to have the waveguide system patterned over a thin Si_3N_4 layer. The fabrication process starts with a standard Si wafer over which is deposited a thick ($1 \mu\text{m}$) SiO_2 layer and subsequently a thin (140 nm) Si_3N_4 one. On top amorphous Si is deposited, annealed to achieve a poly-crystalline structure. Now the waveguide structure

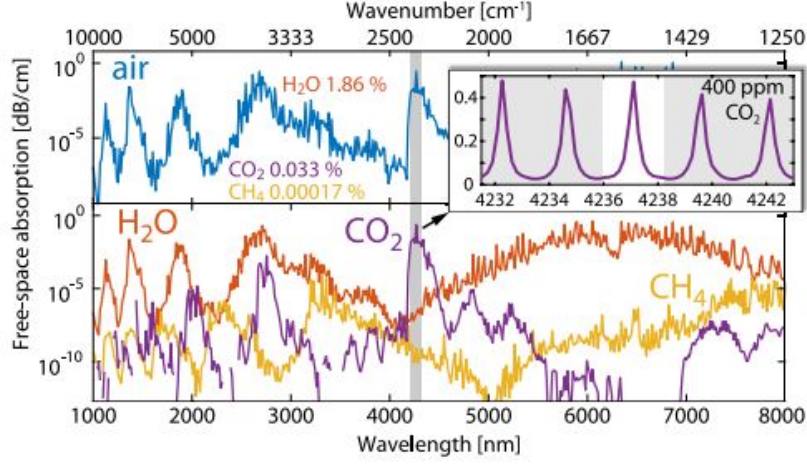


Figure 2.10: Absorption spectra in IR region for CO_2 , H_2O and CH_4 to justify the choice of the operating frequency. [27]

can be patterned on the Si poly-crystalline layer. Finally the Si and SiO_2 are back etched to leave some properly spaced Si/ SiO_2 pillars able to sustain the waveguide and the Si_3N_4 membrane. In such a way the SiO_2 layer is almost completely etched away in order to reduce its related losses and the gaseous sample can be injected both above and below the waveguide in order to increase the interaction volume. The waveguide dimensions are $1400\text{ nm} \times 660\text{ nm}$, chosen to allow two propagating modes: the fundamental quasi-TE mode with $n_{\text{eff}}=2.43$ and $CF=89.3\%$ and the fundamental quasi-TM mode with $n_{\text{eff}}=1.61$ and $CF=73.4\%$ (results obtained by FEM simulations). As shown in figure 2.11, the evanescent field of the latter is also present in the air/gas region below the membrane, this being the reason for the choice of source: a QCL emitting a TM field. The solution proposed in [27] is

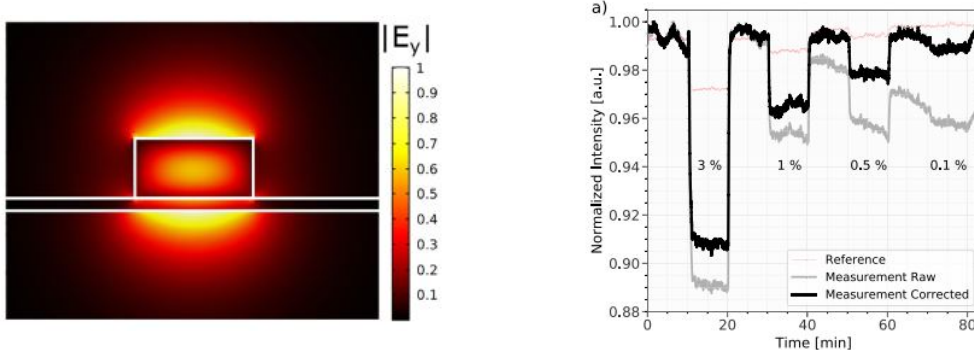


Figure 2.11: **Left:** field distribution for the fundamental quasi-TM mode in the waveguide configuration proposed in [14]. **Right:** time response of the device as different gaseous mixtures are inserted in the sensing chamber.

once again to have a suspended Si waveguide but with some differences. The Si waveguide

is suspended $3\ \mu\text{m}$ above the handler Si substrate by some SiO_2 pillars spaced $83\ \mu\text{m}$ from each other. The waveguide is $2.2\ \mu\text{m} \times 220\ \text{nm}$ except in correspondence of the pillars where it widens to $9\ \mu\text{m}$ with $17\ \mu\text{m}$ linear taper for mechanical support reasons (see figure 2.12). The device is thought to be working at $4.24\ \mu\text{m}$ and equipped with an integrated source, namely a DBF-QCL emitting a TM-polarized beam of light. The absence of a continuous solid bottom reduces the losses and allows the waveguide to be designed with such a thin core. The final result is to have a very low confinement ($CF=53.7\%$ obtained through FEM simulations) allowing large sensitivity. In order to test the performances of the device, the sensing chamber was flushed with pure N_2O and $\text{N}_2\text{O}/\text{CO}_2$ mixtures with different CO_2 concentration every 10 minutes. The obtained results can be seen in figure 2.11. There can be appreciated how concentration down to 0.5% (corresponding to 5000 ppm, a workplace exposure limit in many jurisdictions) can be easily detected.

Before ending this section it is interesting to review the paper [28] which reports about

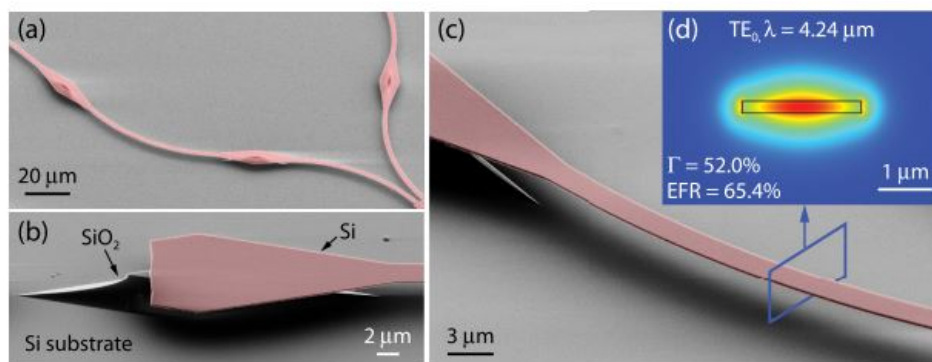


Figure 2.12: Detail of the suspended waveguide structure proposed in [27]. The field distribution for the fundamental mode together with the modal characteristics is shown in the top right inset.

a study on the design of an optimized waveguide section for ultra sensitive measurement. The CF value obtained for example in [27] is very close to the maximum obtainable CF for rectangular shaped waveguide and that an improvement can be obtained by exploiting slotted waveguide. The paper explains that the vertically-oriented slot configuration can present technological problems due to the capability of defining perfect high aspect ratio structures, resulting in possible high scattering losses due to surface imperfections. This is why the Authors indicate that an horizontal slot waveguide is the best solution for ultra sensitive measurement, due to the ability of defining very thin structures with very smooth surfaces. In particular two architectures are proposed having cross section as the one shown in figure 2.14. These particular slot waveguides are optimized to work at $4.7\ \mu\text{m}$ (a characteristic absorption wavelength for N_2O) and with a TM-polarized field. With the optimal values the CF are found to be 41.7% and 32% respectively for the single and double slot configurations. For the double slot solution it is reported that with a $1.44\ \text{cm}$ long interaction region it is possible to detect down to 1 ppm of N_2O concentration, which is an record result, obtained thanks to the high field confinement outside the waveguide and the high absorbance of N_2O .

The measuring circuit is composed by three output branches that split from the main waveguide route through MMI splitters at regular distance intervals. Such a system is able to perform fully on-chip referenced measurement without the need for an external reference apparatus. It was submitted to a similar testing routine with respect to the other device. With the tested configuration of 3.2 mm long waveguide it is demonstrated that concentrations down to 1000 ppm can be easily measured as can be appreciated in figure 2.13. It was calculated that in order to measure the current atmospheric level of CO₂ (at approximately 400 ppm) the optimal length taking into account sensitivity and power loss should be around 1.4 cm.

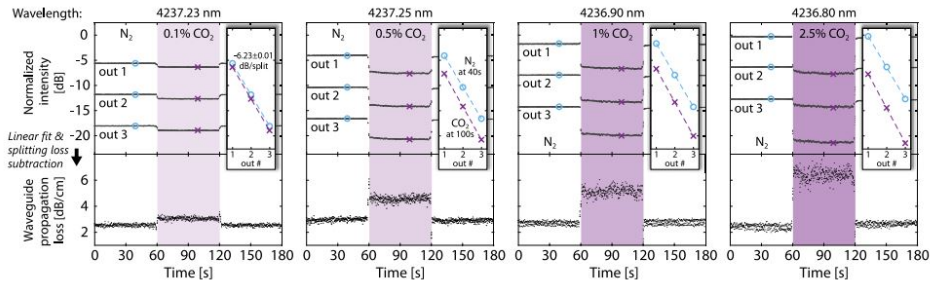


Figure 2.13: Experimental results reported in [27], computed by the evaluation of the three outputs, demonstrating sensitivity down to 1000 ppm

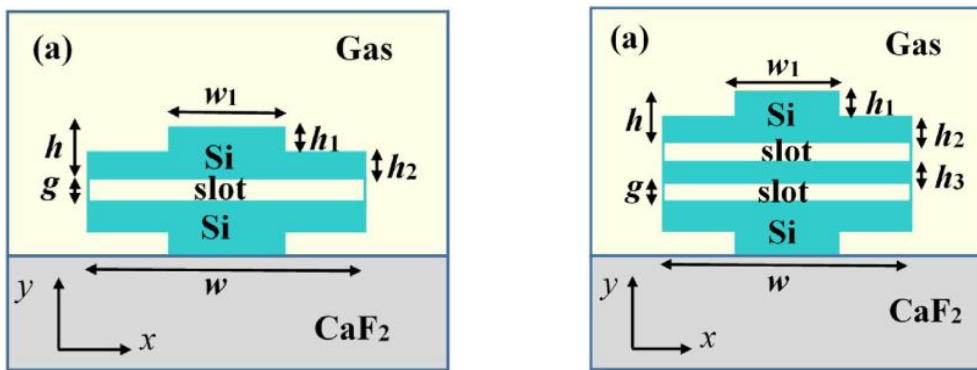


Figure 2.14: Two cross-section solutions for ultra-sensitive devices.[28]

Chapter 3

Multi-branch OPA design and optimization

This last part of my thesis relies on the design and simulation of some building blocks for an Infrared imaging sensor in Silicon Photonics. This device is thought to be working in the healthcare field and due to its small size can be compatible with the existing endoscope probes in the monitoring of backscattered light from a bio-target. The challenging feature that we want to implement is scanless single-pixel imaging. The image of the target will not be acquired by raster scanning of the light beam over it, but by illuminating the target with a sequence of pseudo-random field distributions implemented according some compressed sensing algorithms and subsequent numerical reconstruction to obtain a faster result.

3.1 Materials and wavelength ranges selection

We opted for standard SOI technology and we try to optimize some basic building blocks for the operation in the Mid-Infrared region. The range of possible operation of the device is thought to be $3\ \mu\text{m}$ - $4\ \mu\text{m}$, depending on the laser source used. However for the following simulation the working wavelength is fixed to $4\ \mu\text{m}$, the upper bound for the SOI applications. The device is composed by a QCL emitting in the MIR connected through a non-reciprocal coupler to a multi-branch electrically programmable Optical Phase Array (OPA). All the branches are then connected together in a multi-mode waveguide to generate a pseudo-random field pattern that is radiated and focused with a micro-lens onto the target. The device is then able to collect into a micro-objective the light backscattered by the target and to extract information on its (the target) shape thanks to a detector. This work is focused on the design and optimization of the OPA block and the generation of pseudo-arbitrary field distribution to sense the target, whereas the source and detecting problem will not be treated.

The first issue to address is the choice of the waveguide geometry that is extensively discussed in the next section. Then we go through the design of the OPA block that in particular will be composed by a splitter, a central electrically programmable phase control

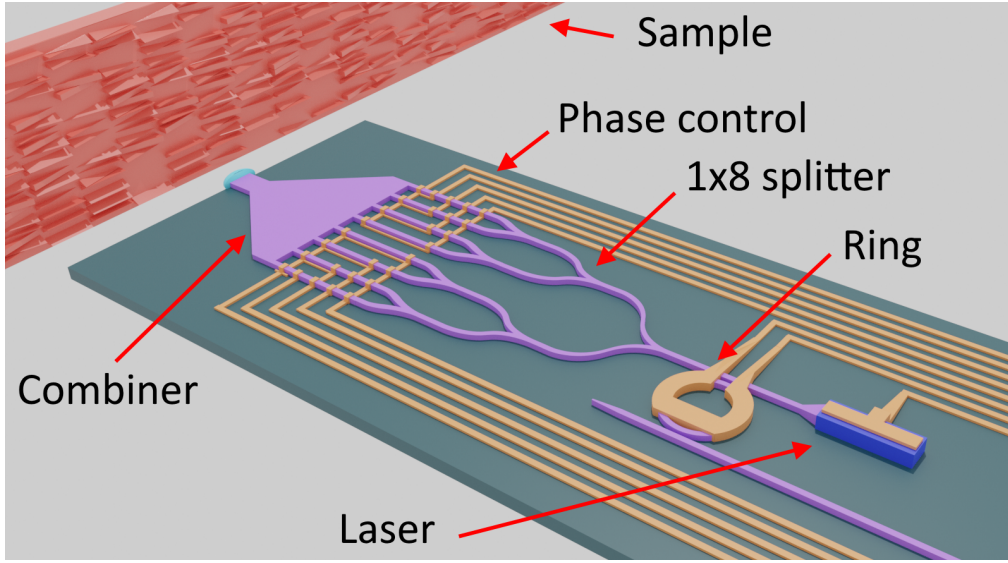


Figure 3.1: Image of the whole device. The laser radiation is first sent to a 1×8 splitter; the phase control section is then used to tune individually the phases of the fields in each waveguide; the resulting fields are recombined by a tapered MMI before illuminating the target. The ring resonator placed right after the laser source is used for monitoring.

region and an output combiner.

3.2 Dispersion relations of a waveguide

In this section are analyzed *waveguides*, how they work and their characteristics. First of all *waveguides* are necessary for this kind of sensor because there is the need of controlling the propagation of electromagnetic waves. This is because in an homogeneous medium the support of a beam of light tends to increase as a consequence of propagation itself. For many application it is instead desired that a beam of light follows a well defined path. To obtain confinement and to allow manipulation of electromagnetic energy one can employ a transversely non-homogeneous structure in order to confine electromagnetic energy through the total internal reflection (TIR).

In this paragraph is briefly analyzed the case of a slab waveguide, the simplest example of dielectric waveguide, because it can be done analytically and one can better understand the basic concepts. A slab waveguide is a stratified structure only in one direction, transverse to the light propagation. A slab of a material having a certain refractive index is sandwiched between two semi-infinite layers of materials (that can be the same, in such cases one speaks of symmetric waveguide) having lower refractive index in the range of application (see figure 3.2). A further approximation is to consider the materials as non-dispersive: its refractive index do not depend on frequency, that can be a good approximation in a small frequency range. The normal approach in electromagnetism is to study the modes of the structure. Modes are field distributions that are solutions of Maxwell's equation in absence of sources and they have the important property of evolve in a simple way in the

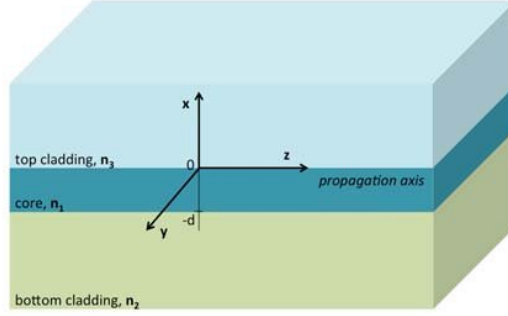


Figure 3.2: Illustration of a typical slab waveguide

propagation into the structure. From this the importance of finding the modes: a generic excitation will be described in terms of the structure modes and the propagation of each term can be done separately in a simple way (a phase shift and an amplitude attenuation) thanks to the linearity of the problem. The modes characteristics can be reported by the so called "dispersion curve", a curve relating the wavelength and the frequency (or their conjugated quantities, the propagation constant $k = \frac{2\pi}{\lambda}$ and the angular frequency $\omega = 2\pi \cdot f$) of an electromagnetic wave inside the waveguide .

The dispersion relation for a slab waveguide can be found analytically by analyzing its transverse section. Two families of modes arises from this analysis, called TE and TM modes, from the property of being constituted of electric/magnetic field transverse to the propagation direction. The clear distinction between TE and TM modes can be done only in this specific case where the system is considered completely independent on one direction (the y-axis in this case). For practical application 3D-dependent structure are employed and as a consequence one do not speak of TE and TM modes, but of quasi-TE and quasi-TM modes that are field distribution in which the electric/magnetic field is predominantly transverse with respect to the propagation direction. The dispersion relation for TE modes is:

$$\frac{\omega \cdot d}{c} \sqrt{n_f^2 - n_{eff}^2} = \arctan \sqrt{\frac{n_{eff}^2 - n_s^2}{n_f^2 - n_{eff}^2}} + \arctan \sqrt{\frac{n_{eff}^2 - n_c^2}{n_f^2 - n_{eff}^2}} + \nu\pi, \quad \nu = 0, 1, \dots \quad (3.1)$$

where d is the dimension of the slab, n_f, n_c, n_s are respectively the refractive indices of the film (the slab), the cladding (the half-space above the film) and the substrate (the half-space below the film), ν is the modal index and n_{eff} is where the propagation constant is hidden: indeed $n_{eff} = k_z/k_0$ that are the propagation constant in the propagation direction and the propagation constant of the wave in free-space ($\lambda_0 = \frac{2\pi}{k_0}$).

This relation (A.1) is valid in the so called "guided regime" that is : $n_c, n_s < n_{eff} < n_f$, that is the range in which a wave actually experiences TIR at the slab boundaries. By writing a computer program one can easily plot that relation and see the changes as some parameter is changed. Some manipulations of the equation has been made to better appreciate the plots: the x-axis is parametrized by a normalized frequency $V = \frac{\omega \cdot d}{c} \sqrt{n_f^2 - n_s^2}$, whereas on the y-axis is reported the effective index n_{eff} . The power of the relation is in the definition

of the the modes that can propagate and their characteristics once the geometry and the materials are defined. In figure 3.3 is reported the dispersion relation for a specific choice of materials and geometry: the film is made from $2\mu\text{m}$ of Silicon sandwiched between two layers of silica; the first $\nu = 5$ modal branches are reported. From the figure can be appreciated how once the system is defined and the operating frequency of the source is fixed (V is fixed) a finite number of modes can be excited and the n_{eff} of each mode is fixed (black dot). Moreover for each mode can be highlighted a cutoff frequency, the V value at which the n_{eff} is equal to n_c (blue dot); below this value of frequency the mode do not exist and as a consequence cannot propagate. It is remarkable how in a symmetric structure the cutoff for the fundamental mode is $V = 0$, this means that the waveguide supports this mode for an arbitrarily low frequency. Moreover it can be noticed how for very high frequency the n_{eff} of the modes tends to n_f with the one of the fundamental mode being the higher. The important matter related to the sensor field is the dependency of the n_{eff} on the refractive index of the cladding. Indeed in the sensor field the cladding in the sensing area can be the analyte, that with its characteristics can change the properties of the waveguide . By forcing a change in the cladding refractive index n_c one can appreciate the change in n_{eff} at a specific frequency. As a consequence the guided wavelength (that is the wavelength in the direction of propagation) $\lambda_g = \lambda_0/n_{\text{eff}}$ varies and give rise to some mismatch that can for example be measured by interferometers as it will be clearer in the following paragraphs.

The following step in the study of a waveguide is the definition of analytical form of the

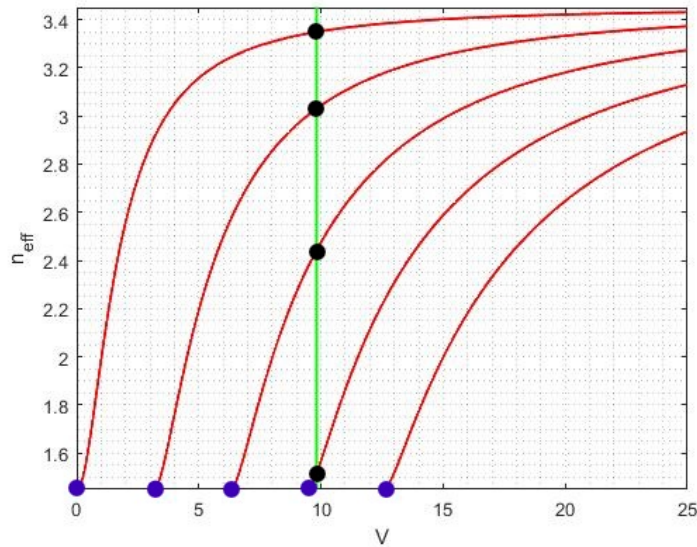


Figure 3.3: Dispersion relation of the first five modes of a slab waveguide . The blue dots represent the cut-off frequency for each mode, whereas the black ones are in correspondence of the n_{eff} of the modes when the frequency is fixed. Graph obtained with the MatLab program in A.1

modes, the field distributions. This can be done by exploiting the transmission line theory applied to the cross section of the slab waveguide . The results of such a computation are

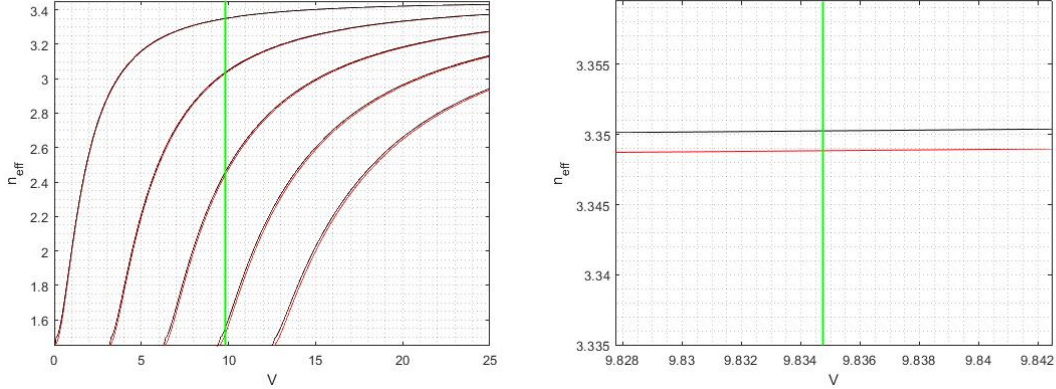


Figure 3.4: Dispersion relations of the first five modes of a slab waveguide with a slight variation in the cladding refractive index . On the right is possible to see a zoom to better appreciate the shift.

reported in figure 3.5 thanks to a Matlab computer program (A.1). The important manner to notice is that the field is not all confined in the film region (delimited by the two vertical red lines), but it extends also in both the cladding and the substrate. These extensions are called *evanescent tails* of the field. As a consequence not all the electromagnetic power is inside the film, but even outside, that is why it is possible to sense what it is outside the film. An important remark to be made is that in this picture no power is propagating in the direction in which the field is evanescent, but, if the mode is above cutoff, only in the direction named z up to now. Finally it is important to define the so called "confinement factor" (CF). The CF is defined as the fraction of power inside the film with respect to all the power carried by the waveguide . The CF is close to 1 when the mode is far from cutoff (high frequency) and it tends to 0 by approaching the cutoff. For communication applications it is desired to have good confinement (CF close to 1), but it will be clearer in the next paragraph how this is not the case for the sensor applications.

The crucial point for the sensor field is that the fields are not perfectly confined inside the film and as a consequence the mode can be affected by what it is outside. A perturbation in the region near the film where the field is not negligible modifies the characteristics of the mode (the effective index and the guided wavelengths). In order to define the limits of this region one has to define the transverse propagation constant $k_t = \sqrt{k_0^2 n_t^2 - k_z^2}$ (where "t" can be cladding or substrate) and the related wavelengths $\lambda_t = \frac{2\pi}{k_t}$. The fields decay exponentially with characteristic length λ_t . If the perturbation is between the film and some λ_t it is said that it can be "sensed" by the waveguide . These characteristic lengths depend on the frequency of operation of the system: at higher frequency λ_t is lower and the field is more confined in the waveguide (CF close to 1).

In sensing application it is desired to have a low CF in order to increase the sensitivity and to sense over a vaster region, in conflict with what happens in the communication world, in which a low CF can correspond to high losses. In this field the CF can be as low as 30% since in evanescent field sensing the aim is to have large sensing region and perhaps high losses (due to absorption in the cladding region).

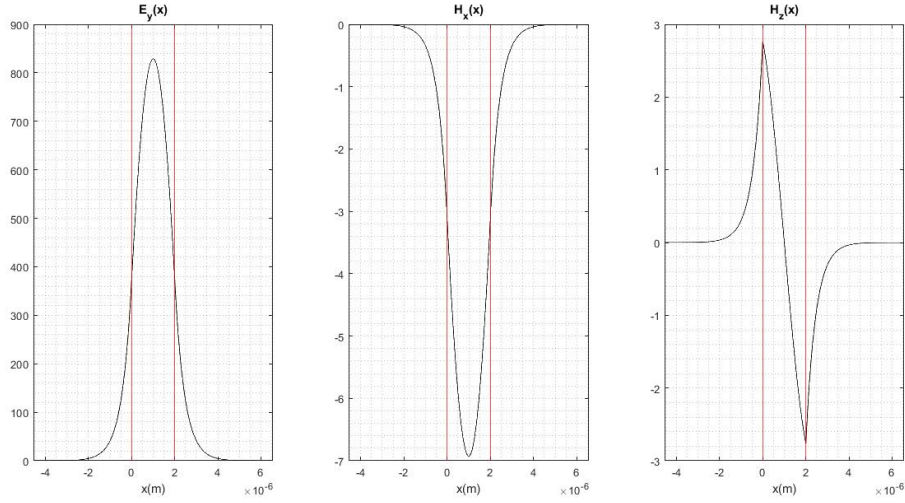


Figure 3.5: Field distributions of the first mode of a slab waveguide . The red vertical lines represent the edges of the core. It is as a consequence evident how the fields extend their evanescent tails outside the core region in the cladding and in the substrate.

3.2.1 Waveguide design

This section is designated to the design flow for the definition of the waveguide geometry for our device. The calculation can still be carried out analytically, but it is much easier to rely on some CAD suite integrating different computational tools. The design is as a consequence carried out entirely relying on the results given by the FEMSim tool in the RSoft CAD suite.

The working free-space wavelength is fixed to $4\ \mu\text{m}$ and the chosen technology is the SOI. For the design of the cross-section of the waveguide we take two parallel ways: a rectangular solution with height fixed to the standard $220\ \text{nm}$ and a square solution. In order to decide for the optimum solution we carried out some simulations to compare the guiding parameters of the various geometries. In particular we are interested in defining a geometry that is able to sustain a single mode in a range close to the working λ . Consequently the implemented simulations have the objective to calculate the real and imaginary part of the n_{eff} for the first three modes. To do that it is sufficient to start a new project in the RSoft environment, define the core, cladding and substrate materials (namely Silicon and Silica) and insert a straight segment with unitary length. Exploiting the FEMSim simulation tool it is possible to extract the modal characteristics (n_{eff} for our purposes) for a defined number of modes starting from the fundamental (three modes are the one we need in this case).

Concerning the squared cross-section solution, we tested waveguides with side dimensions from $1\ \mu\text{m}$ to $1.5\ \mu\text{m}$. The obtained results for the first and the third mode are reported in figure 3.6. Remark: being the structure symmetrical, the first two modes will be degenerate. The plots show how the first mode is strongly guided (n_{eff} higher than the refractive index of Silica) for every chosen dimension in all the considered λ -range, whereas the third one is guided only up to $4\ \mu\text{m}$ for side dimension up to $1.1\ \mu\text{m}$ as the curve flattens for

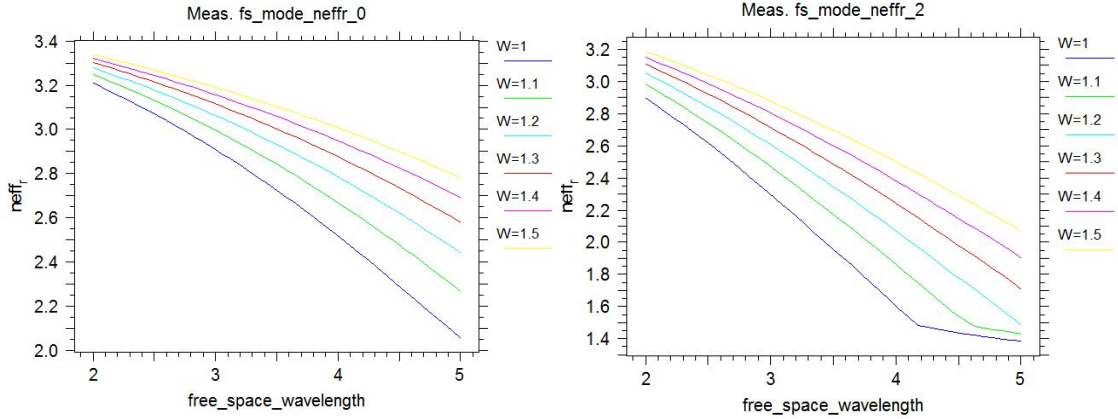


Figure 3.6: **Left**: dispersion relations of the fundamental mode of a squared waveguide with different dimensions. **Right**: dispersion relations of the third mode of a squared waveguide with different dimensions. Please note the flattening of the blue curve (associated to side dimension of 1 μm) at high free-space wavelength, clear sign of a mode below cut-off.

high λ . Concerning this first solution as a consequence the optimal side dimension is 1 μm , ensuring the lowest possible number of guided modes together with good confinement of the first one.

Moving to the fixed height solution, we performed similar simulation to find the optimal waveguide width (W) taking into account the height fixed to 220 nm. In figure 3.7 are reported the calculated dispersion relations for the first and the second mode with W spacing in the range 1 μm -3 μm . The optimal W value is found to be 2 μm . Indeed the

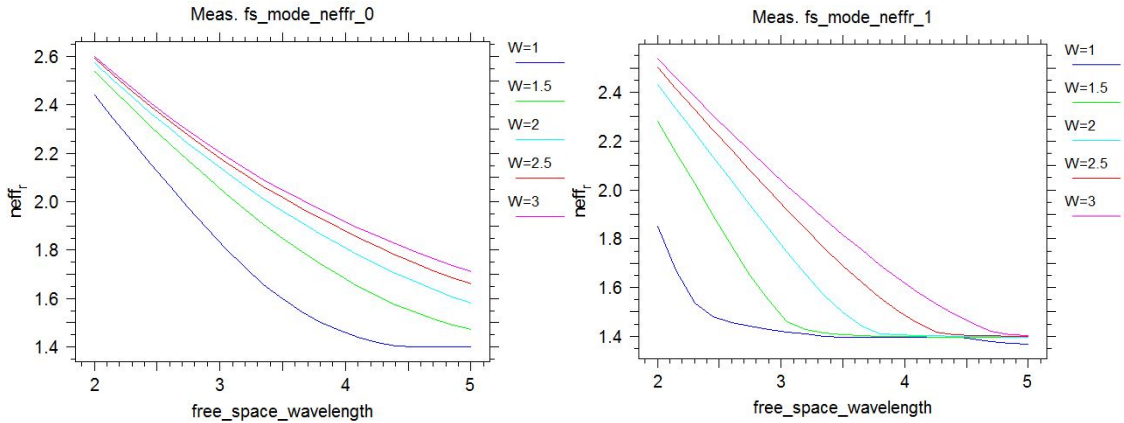


Figure 3.7: **Left**: dispersion relations of the fundamental mode of a rectangular waveguide (height fixed to 220 nm) with different widths. **Right**: dispersion relations of the second mode of a rectangular waveguide (height fixed to 220 nm) with different widths.

waveguide is single mode near the working λ (as it will be for lower W values) and have a good confinement. With lower W values the fundamental mode is too poorly confined leading to larger losses (remember that the working frequency is near a region of strong

absorption for the Silica); with larger W values on the contrary the waveguide becomes multi-modal with all the associated problems.

Finally the waveguide geometry is fixed to $220\text{ nm} \times 2\text{ }\mu\text{m}$, taking advantage of the standard SOI overlayer height and by selecting the minimum width to ensure good confinement and single-mode operation according to FEMSim simulations.

Up to now the simulations have taken into account only the modal losses due to poor confinement. In order to compute the losses due to material absorption we use the qualitative formula: $L_{\text{tot}} = L_{\text{Si}} \cdot CF + L_{\text{SiO}_2} \times (1 - CF)$, where the CF can be obtained by some further simulation in RSoft and the losses due to Silica are taken from [6], while the losses associated to Silicon are considered negligible. The CF can be easily found in Rsoft by inserting a monitor at the end of the waveguide and setting it in "Overlap" mode with respect to the input field. The straight waveguide is fed by the computed fundamental mode of the previous step and through the BEAMProp simulation tool the mode is propagated up to the monitor. The computed CF is found to be close to 70%, fixing the losses to: $L_{\text{tot}} = 5\text{ dB cm}^{-1} \times (1 - 0.7) = 0.35\text{ dB mm}^{-1}$.

Going back to the core of our design, the task of the OPA is to generate an electrically controllable field distribution that will be needed to implement scanless imaging. This task can be implemented by splitting the light incoming from the laser source in a sufficiently high number of waveguide branches. Each branch is provided with a electrical (thermal) control region in order to provide individual phase-shifts to control the final field pattern. All the branches are then combined together into a multi-mode waveguide and finally to the emitting micro-lens to generate the pseudo-random field distribution [29]. In order to study this problem we use the BEAMProp simulation tool inside the RSoft environment (based on a finite difference beam propagation method). The problem of designing the whole structure is carried out by analyzing the different building blocks separately. In the following paragraphs is described the design flow for the optimization of the splitter and combiner right after the definition of the technological and geometrical characteristics of the thermal control region.

3.3 Thermal control region

As it will be explained subsequently, it makes sense to start the design process from the study of the thermal control region. For the phase-calibration, we opt for thermo-optical effect as it induces no additional optical losses per se and it is easy to implement from the technological point of view. Indeed metal heaters can be defined by a standard lift-off process, as a consequence obtaining metal line (namely TI/Au alloy, but any other CMOS compatible metal can be used) of $2\text{ }\mu\text{m} \times 220\text{ nm}$ of cross section with a defined length on the Silica substrate is not a big issue. The goal of this block is to allow the possibility of inserting the desired propagation delay in a specific branch without affecting the other branches. Fixing the length of the waveguide can be a good departure point in order to fix the Δn_{eff} to induce in the mode to cause the wanted phase-shift. From this it is possible to compute the needed Δn (of the Silicon waveguide) and ΔT (in the metal strip). If the final results are consistent with the technological environment we are using one can consider the tested set of parameters as a possible solution for our need.

The RSoft Multi-physics tool, in particular the thermo-optic module, was used in order

to perform the necessary simulation. It is sufficient to define the cross-section of the structure one wants to analyze and fix the temperature of one or more components (in terms of ΔT with respect to the standard working temperature of the system) to extract the information on Δn and ΔT in the domain of interest. The analyzed structure is composed by the $2\ \mu\text{m} \times 220\ \text{nm}$ Si waveguide, a $2\ \mu\text{m} \times 220\ \text{nm}$ Au strip $3\ \mu\text{m}$ apart in the X-direction and another $2\ \mu\text{m} \times 220\ \text{nm}$ Si waveguide (playing the role of a generic adjacent waveguide branch for cross-talk study) $16\ \mu\text{m}$ apart in the X-direction, all surrounded by Silica.

An example of final result of this analysis is reported in figure 3.8. Here the ΔT is fixed to $50\ \text{°C}$ according to what can be normally seen in this type of systems [29]. In figure it can be appreciated how the waveguide close to the Au strip undergoes a change in the refractive index $\Delta n = 0.002$ corresponding approximately to 1‰ of the initial value, whereas the other waveguide is practically insensitive to the T variation. To better appreciate these facts we performed multiple FEMSim simulations taking advantage of the MOST scan tool in RSoft scanning the ΔT parameter in the $0\ \text{°C}$ - $50\ \text{°C}$ range, to see the n_{eff} changes of the fundamental mode of the Si waveguide. The results concerning both the close and the

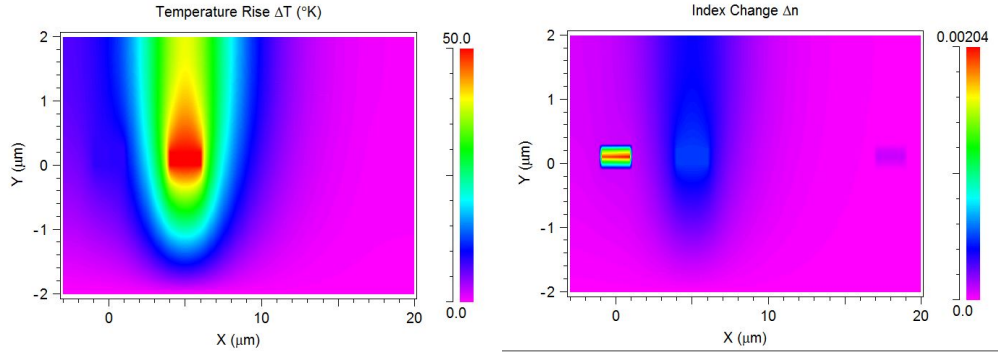


Figure 3.8: Temperature variation ΔT (left) and refractive index variation Δn (right) in a transverse cut as the temperature increase of the metal strip is fixed to $50\ \text{°C}$. One can appreciate how the refractive index of the close waveguide is clearly modified, whereas the one of far apart waveguide is slightly touched (remember that in figure the spacing is fixed to $17\ \mu\text{m}$, when in the final configuration the distance will be $25\ \mu\text{m}$)

far apart waveguide are reported in the left and right plot of figure 3.9 respectively. Here we can see how the n_{eff} of the close waveguide varies starting from its third decimal digit with a relative final variation in the order of 1‰. Concerning the other waveguide this change is limited to the fourth decimal digit. Such an n_{eff} variation can be transformed approximately in a phase variation along the 1 mm long section by applying the following formulas:

$$\lambda_{z,0} = \frac{\lambda_0}{n_{eff,0}} = 2.212\ \mu\text{m} \quad NumWav_0 = \frac{1000\ \mu\text{m}}{\lambda_{z,0}} = 450.05$$

$$\lambda_{z,50} = \frac{\lambda_0}{n_{eff,50}} = 2.209\ \mu\text{m} \quad NumWav_{50} = \frac{1000\ \mu\text{m}}{\lambda_{z,50}} = 450.69$$

in which using the effective index approximation we calculate the number of wavelength (in the z-direction) contained in a 1 mm long straight segment for the two situation being

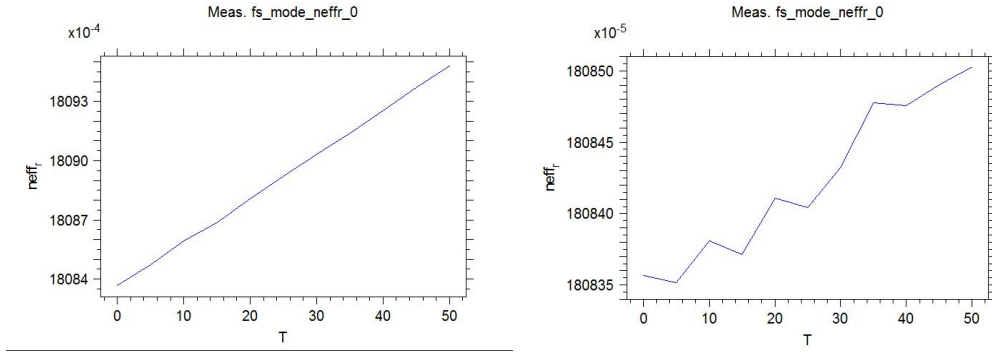


Figure 3.9: **Left:** Δn_{eff} of the fundamental mode of the waveguide close to the metal strip. **Right:** Δn_{eff} of the fundamental mode of the waveguide far from the metal strip. (Please note the different scales)

0°C and 50°C temperature offset. Clearly in the second case more than half a wavelength is obtained and as a consequence our goal of π phase-shift is completely fulfilled.

In order to further lower the cross-talk between adjacent branches, their distance is fixed to 25 μm . Another change that can be implemented is to get closer the metal strip and the waveguide in order to increase the thermal control and lower the distance needed to obtain the same phase-shift or vice versa lower the ΔT needed to always obtain the same phase-shift. This route is not further investigated because by placing the metal strip too close to the waveguide unwanted losses due to metal absorption can occur, due to the non perfectly confined nature of the guided field [29].

3.4 Optical splitter

The second analyzed block is the splitter, realized in the first place using the standard y-splitter scheme. Implementing a fractal scheme, from a single y-splitter stage it is possible to generate a number of output equal to a power of two. The study starts from a 1-to-2 splitter, being this the first stage for the cascaded 1-to-8 splitter. It is composed by an input straight segment followed by a segment with increasing tapered width to match the two S-shaped output branches. The parameters to optimize in this structure are the length of the tapered section L_{tap} and the horizontal (DX) and longitudinal (DZ) sizes associated to the surrounding box of the S-shaped branches in order to ideally obtain a 50-50 power split in the two output branches. DX and DZ are strictly related one to the other since larger values for the DX displacement requires larger DZ values to ensure low losses. Here the point is to fix DX for our need and find the minimal DZ in order to minimize the bending losses, thus minimizing the splitter footprint. The DX value can be fixed knowing that the final spacing between each branch required to ensure a satisfactory independent control is fixed to 25 μm as already discussed in the previous section. According to the scheme in figure 3.1, the DX displacement that the first stage must ensure is twice this spacing, imposing therefore DX=50 μm . Now the next step is to find the minimum DZ in order to limit the bending losses and the value for L_{tap} to ensure 50-50 split. This optimization can be done in the Rsoft environment by calling the MOST optimizer tool, that minimizes a

function by sweeping one or more parameter in a given range. In this case the function that we want to minimize is $y = 1 - P_{out,1}$ where $P_{out,1}$ is the power calculated at the end of the "Pathway monitor" inserted in the upper path (that for symmetry reasons will be equal to the one at the end of the lower path). The parameters given to the minimization tool are L_{tap} and DZ , sweeping in the ranges $25\ \mu\text{m}$ - $50\ \mu\text{m}$ and $150\ \mu\text{m}$ - $500\ \mu\text{m}$ respectively. A final remark prior to the obtained results is that the field used as input is the fundamental mode calculated in section 3.2.1 and invoked in the "Launch field" field. The optimal results regarding our parameters can be found in the table 3.1, where the value coming from the RSoft optimization are reported together with the final value used in further simulations. We choose to approximate the L_{tap} value to $40\ \mu\text{m}$ since no difference in power arriving

Table 3.1: Optimal values for the 1-to-4 splitter coming from MOST optimization in RSoft

Parameter	RSoft optimal value	Final value
L_{tap}	39.435 64 μm	40 μm
DZ	483.576 74 μm	250 μm

at the end of the branches can be appreciated with respect to the optimized situation. Moreover concerning DZ , the simulation clearly gives a value close to the higher limit of the given range because it minimize the bending losses, however we choose to reduce DZ to $250\ \mu\text{m}$ in order to reduce the propagation losses and still having negligible bending losses. Once the 1-to-2 splitter is optimized to our need the next analyzed structure are the 1-to-4 and 1-to-8 splitters, obtained from the results achieved in the first analysis. Concerning the 1-to-4 structure we consider as fixed the parameter related to the first y-splitter and we focus on the ones related to the second splitting stage. Here we define again $L_{tap,2}$, DX_2 and DZ_2 as before, with the 2-subscript to identify that these quantities refer to the second splitting stage. As before, DX_2 can be fixed to $25\ \mu\text{m}$ with similar considerations to the previous case. As a consequence, since the displacement in X-direction is half with respect to the first stage, DZ_2 is fixed to $125\ \mu\text{m}$ ($=0.5 \times DZ$). The attention is focused in the optimization of the other parameter exploiting again the MOST tool and sweeping $L_{tap,2}$ in the range $40\ \mu\text{m}$ - $60\ \mu\text{m}$. The obtained result is: $L_{tap,2}=53.868\ \mu\text{m}$. The same reasoning carried out previously does not apply to $L_{tap,2}$ as substantial changes in the splitting proportion can be seen as its value changes by a small margin. The circumstance is studied by recording the "Pathway monitor" values beyond the second splitting stage for two branches belonging to the same sub-branch. This can be done by exploiting the MOST tool in "Scan" condition, which performs simulations and records one or more results given one or more sweep parameters (in our case $L_{tap,2}$ is swept in the range $52\ \mu\text{m}$ - $55\ \mu\text{m}$). What we want to measure is the difference in power arriving at the end of sub-branches belonging to the same branch; the obtained results are reported in figure 3.10 where it is clearly visible that an ideal value exists for $L_{tap,2}$, where the input power is exactly divided between the two sub-branches; moreover, it is possible to observe that variations as big as $100\ \text{nm}$ cause a negligible variation in the power unbalance, making this design extremely insensitive to fabrication tolerances.

Finally, the 1-to-8 splitter was designed in a similar way (scheme reported in figure 3.11). The parameters to optimize are reported in table 3.2 with their associated optimal values. The DX_3 and DZ_3 value are fixed following the previous remarks. Concerning the other

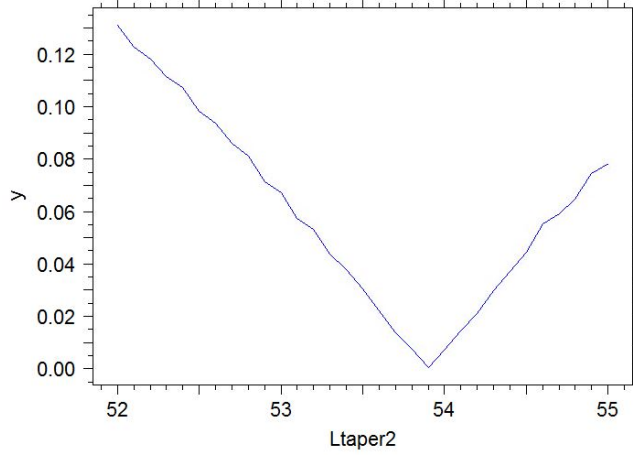


Figure 3.10: Power difference in two sub-branches belonging to the same branch normalized to the power at the input port as a function of the $L_{tap,2}$

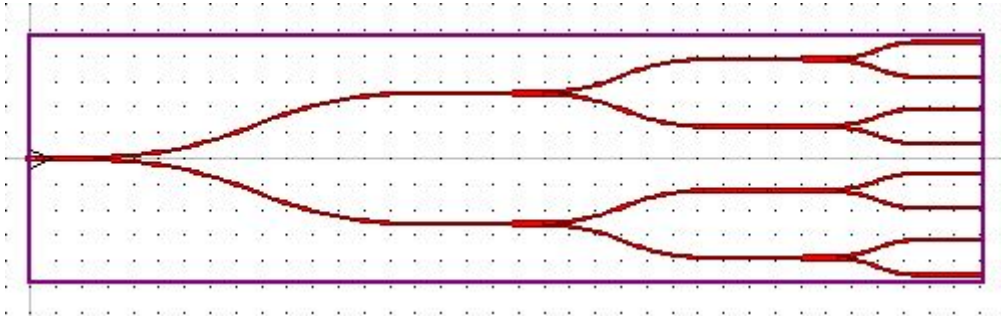


Figure 3.11: Schematic of the final 1-to-8 splitter obtained in the RSoft environment

two parameters on the other hand we resort to a two variable MOST optimization with the final aim of having equal power confined in each branch. To do that the confined power is sensed along 4 different pathways. The result of a simulation with all the parameters to their optimal values is reported in figure 3.12. Here it can be appreciated the power balance between each branch, remarking that the power is normalized to the input port. At the far end of each branch it is measured 10% of the input power; these 1 dB losses can be associated to the bends and to the fact that the input mode used as excitation is the fundamental one calculated with FEMSim simulation, being slightly different to the BEAMProp one.

3.5 Design of the MMI

The next analyzed structure is the MMI. Here MMIs are studied for splitting purposes, but they will be re-evaluated in the next section also for combining purposes. MMIs can be interesting for their capability to split the input field at a lower distance with respect to

Table 3.2: Optimal values for the 1-to-8 splitter coming from MOST optimization in RSoft

Parameter	RSoft optimal value	Final value
DX_3	/	12.5 μm
DZ_3	/	62.5 μm
$L_{tap,2}$	49.771 31 μm	/
$L_{tap,3}$	53.507 73 μm	/

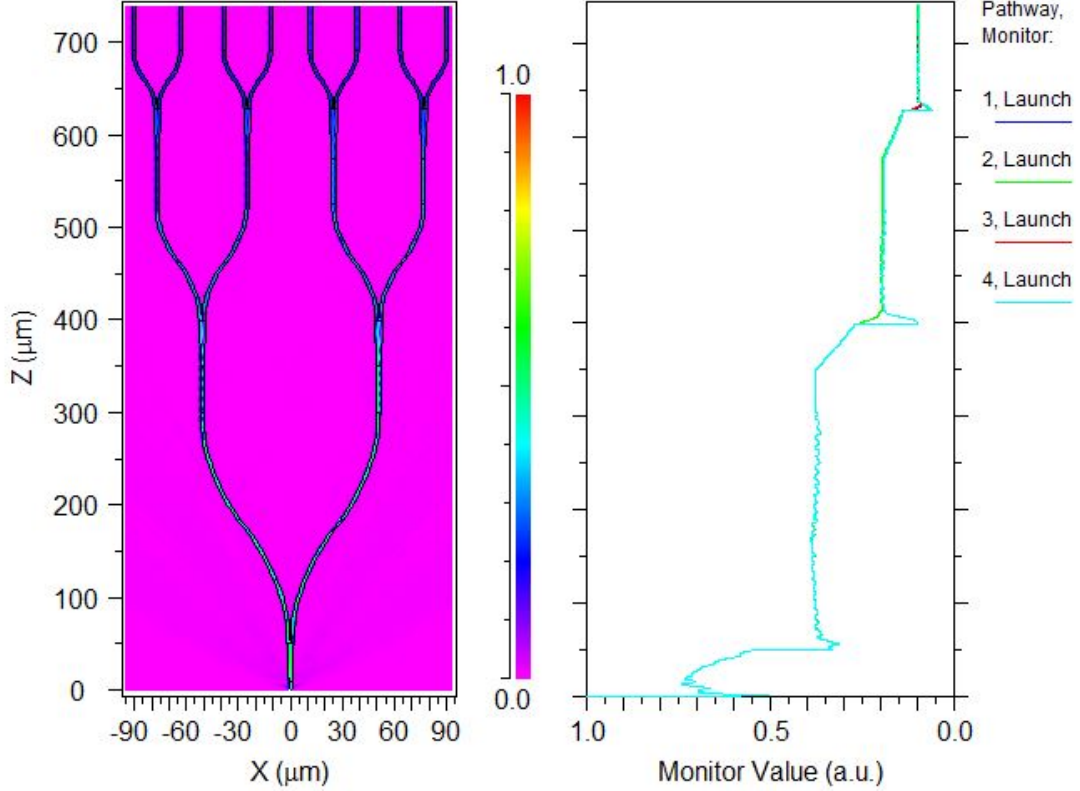


Figure 3.12: Simulation results for the optimized 1-to-8 splitting structure, in which can be appreciated the good balance between each branch. ("Launch 1, 2, etc" are the normalized power in different branches)

other devices like for example the tapered junction used up to now and this can be crucial in our application. To demonstrate this feature we design another 1-to-4 splitter along the same line as the previous one, but substituting the tapered segment in correspondence of each y-junction with an MMI. In particular this MMI will be a waveguide segment with increased width with respect to the standard single-mode ones. Its width is fixed to four times the standard width ($W_{MMI} = 8 \mu\text{m}$). The MMI segment is previously individually tested to optimize its parameter and than will be placed in the 1-to-4 splitter project. The parameter to optimize with their associated optimal value are reported in table 3.3. L_{MMI} is the length of the MMI segment, whereas X_1 is the position of the output segment with respect to the center of the MMI segment. Finally this MMI block can be inserted in the

Table 3.3: Optimal values for the 1-to-2 MMI splitter coming from MOST optimization in RSoft.

Parameter	RSoft Optimal value
L_{MMI}	$18 \mu\text{m}$
$X1$	$2.15 \mu\text{m}$

1-to-4 splitter project to test its ability. In figure 3.13 are reported both the scheme and the value of the "Pathway monitors" for different branches. It can be appreciated how the second stage MMI does not actually split the incoming power 50/50.

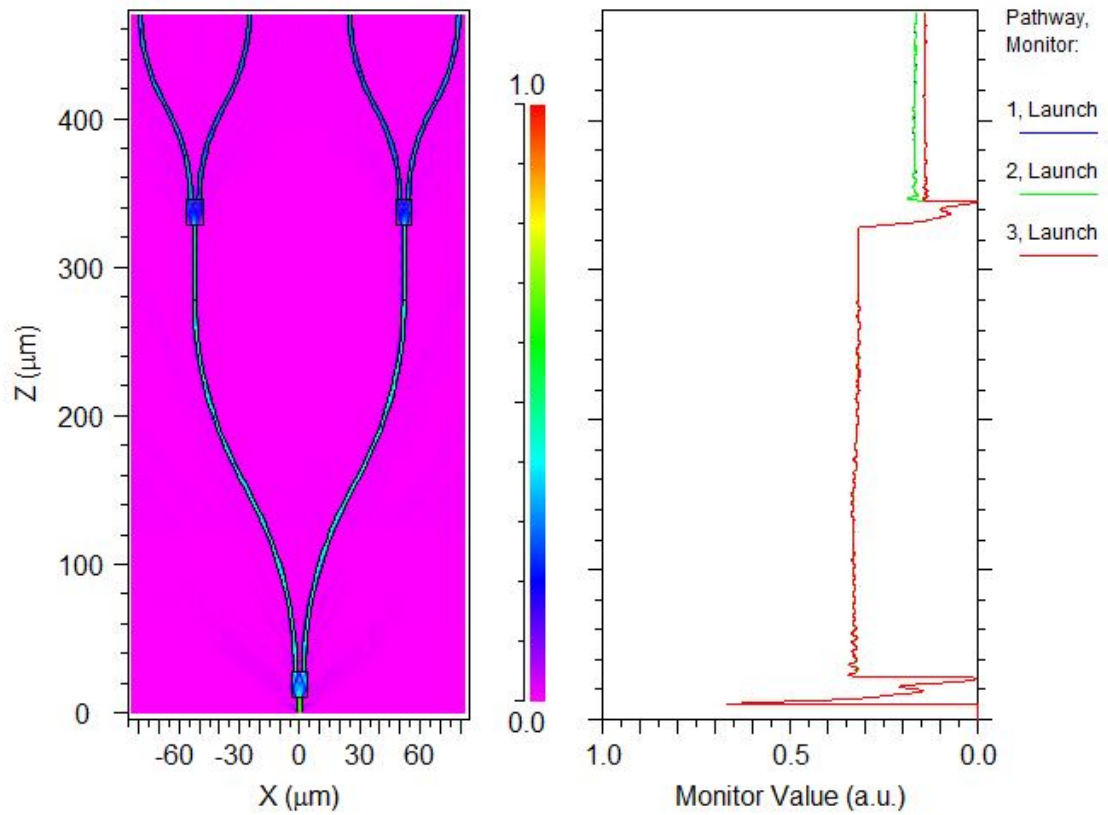


Figure 3.13: Simulation results for the 1-to-4 splitter exploiting MMIs. This results shows how there is a not perfect balance in the second splitting stage.

3.5.1 Combiner

In order to start the dissertation about the combiner block, a further discussion is necessary about the goals we want to achieve. Up to now we have discussed the methods to split the input power in a certain number of branches. The field in each branches, before reaching the combiner block, will undergo a certain electrically programmable and path dependent

phase-shift. The aim of the combiner block at this point is to merge all the incoming signal having different phases in a single multi-mode waveguide , in order to generate a pseudo-random field distribution at the far end. It is crucial that the output waveguide of the combiner block is a multi-mode one, in order to preserve the characteristic interference pattern of field having different phases. Indeed, this will allow to find in output a far field pattern whose profile in the horizontal plane can be thermally controlled.

To implement such a combining function the first object that comes to mind is the MMI. In this direction the previous simulation concerning the optimization of a 1-to-2 MMI can come in handy. In this section we will start the optimization from the design of a 4-to-1 MMI, ending with a 8-to-1 MMI.

In order to design a 4-to-1 MMI, we started with the optimization of a 1-to-4 MMI splitter, taking advantage of the reciprocity of the structure. By considering this inverse structure it is easy to optimize the needed parameter. The analyzed structure is composed by a straight input waveguide , a central MMI region and four output segments. The MMI region width is fixed to 10 times the width of the single-mode waveguide . Moreover the structure is fully described once the length (L_{MMI}) of the MMI region, X_1 and X_2 (being the lateral offsets of the waveguide segments with respect to the center of the MMI) are defined (see the left-most image in figure 3.14). The L_{MMI} we are searching for is the distance at which we can find four equal peaks in the characteristic interference pattern of an MMI device with symmetric excitation (restricted interference). By assuming effective index approximation it can be analytically calculated as one fourth of the self imaging length. On the other hand the value can be found with a 3D BPM simulation. Once L_{MMI} is fixed the other parameters can be optimized by means of a MOST optimization. To do that one has to define only two pathways (taking advantage of the symmetry of the structure) with the two right-most waveguides output and find X_1 and X_2 to maximize the output power in each branch. The obtained results are reported in table 3.4.

Once the structure has been optimized in the splitting regime it is sufficient to reverse it

Table 3.4: Optimal values for the 1-to-4 MMI splitter coming from MOST optimization in RSoft.

Parameter	RSoft Optimal value
L_{MMI}	55 μm
X_1	2.557 62 μm
X_2	7.973 21 μm

and characterize its behaviour in the combining one. At each of the four input waveguide it is applied a field distribution being the fundamental mode found in 3.2.1. An interesting feature of the RSoft software is that it is possible to apply a different phase shift to each input field. By simply varying the relative phases of the signals coming from the different we want to calculate the field distribution at the end of the 50 μm long multi-modal output waveguide. RSoft can give a polar plot representation of the far-field intensity at the end of the output waveguide. Exemplary far-field plots obtained with different phase parameters can be seen in figure 3.14. The first remarkable fact is that the higher interference intensity peak of the structure is always at a distance L_{MMI} (but this should not be a surprise due to the reciprocity of the structure). Secondly it is remarkable how with different phase

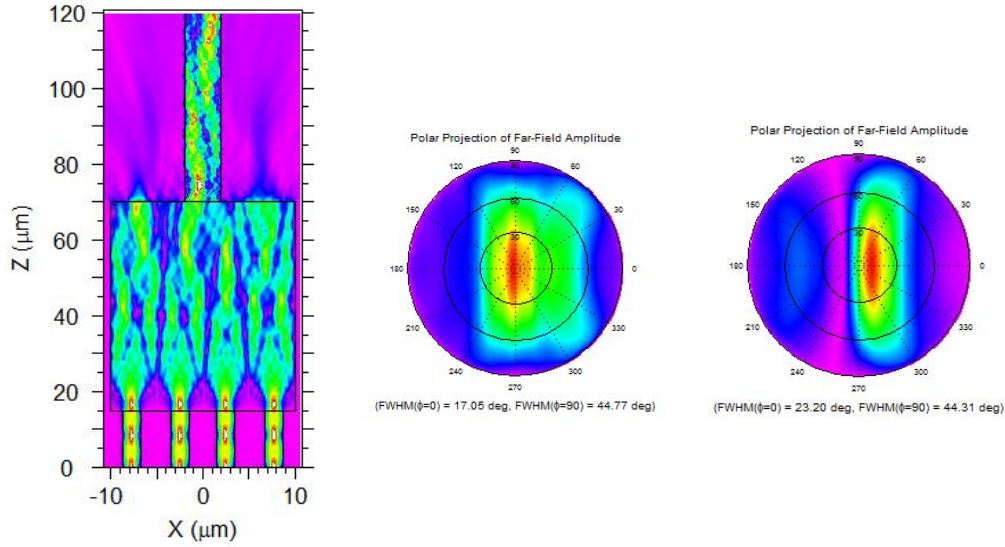


Figure 3.14: **Left:** BEAMProp simulation results of the 4-to-1 MMI combiner with random input phases. **Middle and right:** far field distributions obtained with two different set of input phases to demonstrate the beam steering capability of the system.

parameter configuration it is possible to spatially shift the far-field peak, proving the beam steering capability of such a structure. Together with the polar plot also a FWHM parameter is reported, which is the amplitude in degrees of the main lobe. From simply running multiple simulation it is not easy to see a pattern in the correspondence between the phase parameters and the far field pattern. This topic will be more extensively treated in the following section. However some final remarks that can be made in connection with figure 3.14 are:

- the possible steer angle is limited to $\pm 15^\circ$;
- only a single lobe is present.

Finally from the plots in figure 3.14 it is evident how a considerable amount of power can be lost with such a rectangular MMI configuration. This is why in figure 3.15 a different MMI solution is proposed with a tapered central section that merges with the output waveguide with no discontinuity in order to radiate a larger amount of power. All the geometrical parameter are the same as before. Here once again it is not easy to highlight a pattern between the phase parameters and the far-field distribution, but at the same time it can be appreciated how a larger steering capability can be achieved ($\pm 25^\circ$) together with the possibility to obtain side-lobes. These are features that will be readdressed in section 3.6. Proved the beam-steering capability of the 4-to-1 combiner it is useful to investigate the capability of an 8-to-1 MMI combiner. Once again the geometrical parameter optimization is carried out using the MMI in "reverse" configuration due to the easiness of the problem. The obtained optimal values are reported in the table 3.5. For energy confinement reasons we decided to opt directly for the tapered MMI geometry as can be appreciated in figure 3.16. The input channels are named IN1, IN2 and so on starting from the top-most. Finally

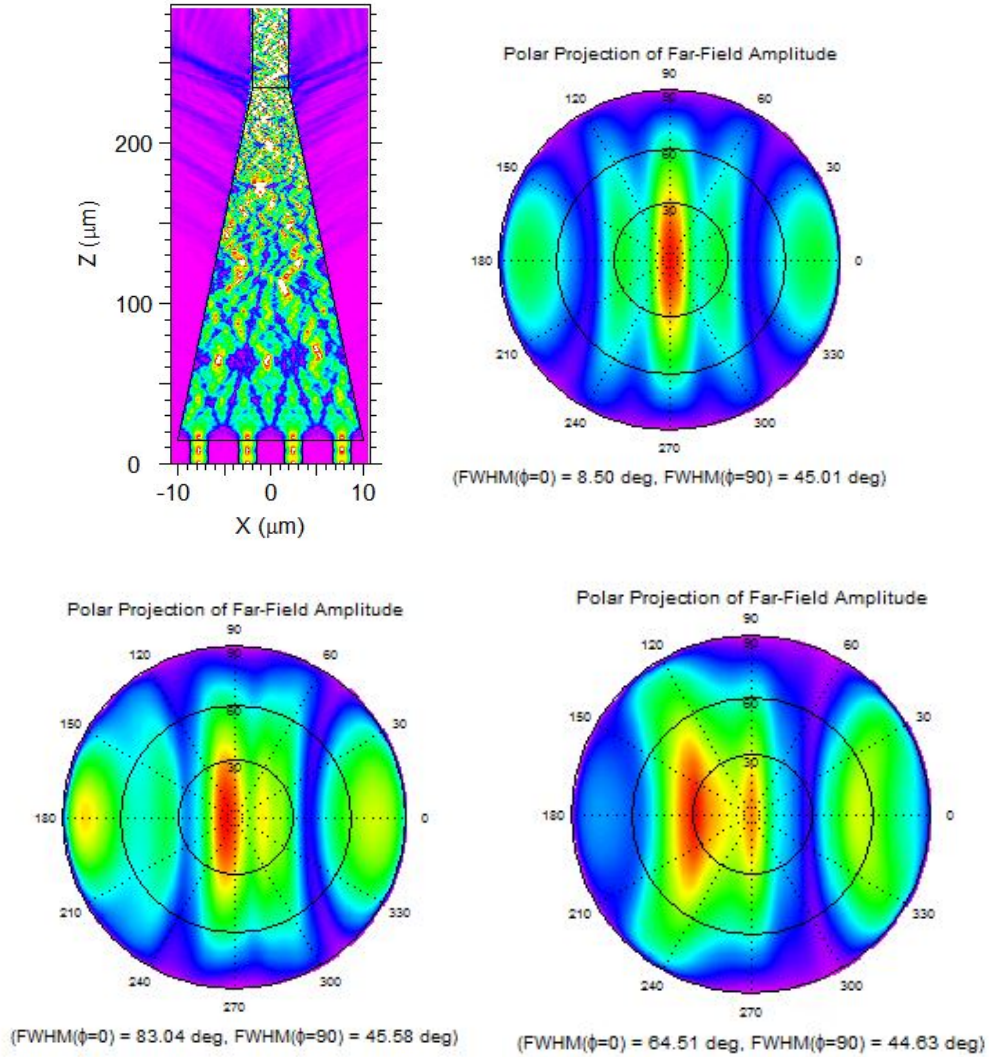


Figure 3.15: **Top-left:** BEAMPROP simulation results of the 4-to-1 MMI combiner with tapered width and random input phases. **Top-right:** far-field distribution obtained with zero relative phase-shift between the branches. The result is a symmetrical, single (narrow) lobe response. **Bottom:** far-field distributions obtained with random input phase-shift to demonstrate the possibility of obtaining many significant output lobe at different propagation angles.

at each input branch is associated a field distribution equal to the fundamental mode of the waveguide found in 3.2, with the possibility to define an individual phase shift for each branch through the change of a parameter. In figure 3.17 are reported some polar plots for the far-field intensity related to different phase parameter for the eight branches. In particular the first image is obtained with all the phase shift parameter fixed to the same value (namely 0°). In such case the output is clearly symmetrical with respect of the

Table 3.5: Optimal values for the 8-to-1 MMI combiner with tapered width coming from MOST optimization in RSoft

Parameter	RSoft Optimal value
L_{MMI}	96 μm
W_{MMI}	40 μm to 4 μm
X_1	2.5 μm
X_2	7.5 μm
X_3	12.7 μm
X_4	17.8 μm

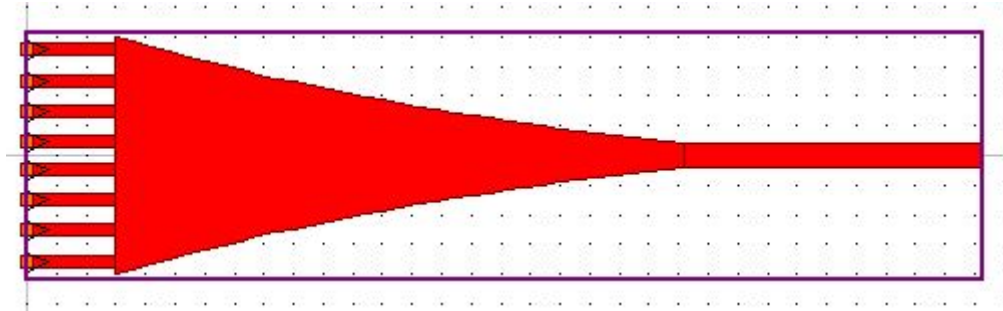


Figure 3.16: Schematic of the final 8-to1 MMI tapered combiner obtained in the RSoft environment

z-direction, with a very thin main lobe and two side-lobes with lower peak power. On the side it is present a similar result obtained with just the insertion of a 30° phase shift at port IN1, leaving all the others as before. The obtained far field distribution resembles the first one, with the slight difference that some power is transferred to the right side-lobe. The recognition of a pattern gets even more complicated when a pseudo-random phase shift is applied to all the input ports at the same time. Look for example at the two plots reported in the bottom part of figure 3.17. They differ only by a phase-shift of 15° at port IN2, but the power peak can be found at a completely different ϕ angle.

As a consequence of these results, at this point it is meaningless to speak about the beam steering capability of such a structure, since we are no more in front of a single lobe response which direction can be tuned according to the needs. It is more recommended to speak about a structure able to generate a certain field distribution having a tunable amount of peaks with tunable dimensions and peak power, which characteristic can be controlled by controlling the phase of each branch. Furthermore we can state that by increasing the number number of input from four to eight the degrees of freedom are magnified. A similar increase in the freedom in the definition of the far-field distribution is expected as the number of input is further increased. Finally concerning the function linking the input phase-shifts to the final field distribution we can say that can't be easily extracted by simply performing multiple simulations or by carrying out some analytical calculation. This problem can be treated exploiting a deep learning approach based on a multi-layered neural network. Indeed as it is reported in [33] in recent years deep learning methods have attracted great interest in the optical community for the direct and reverse design

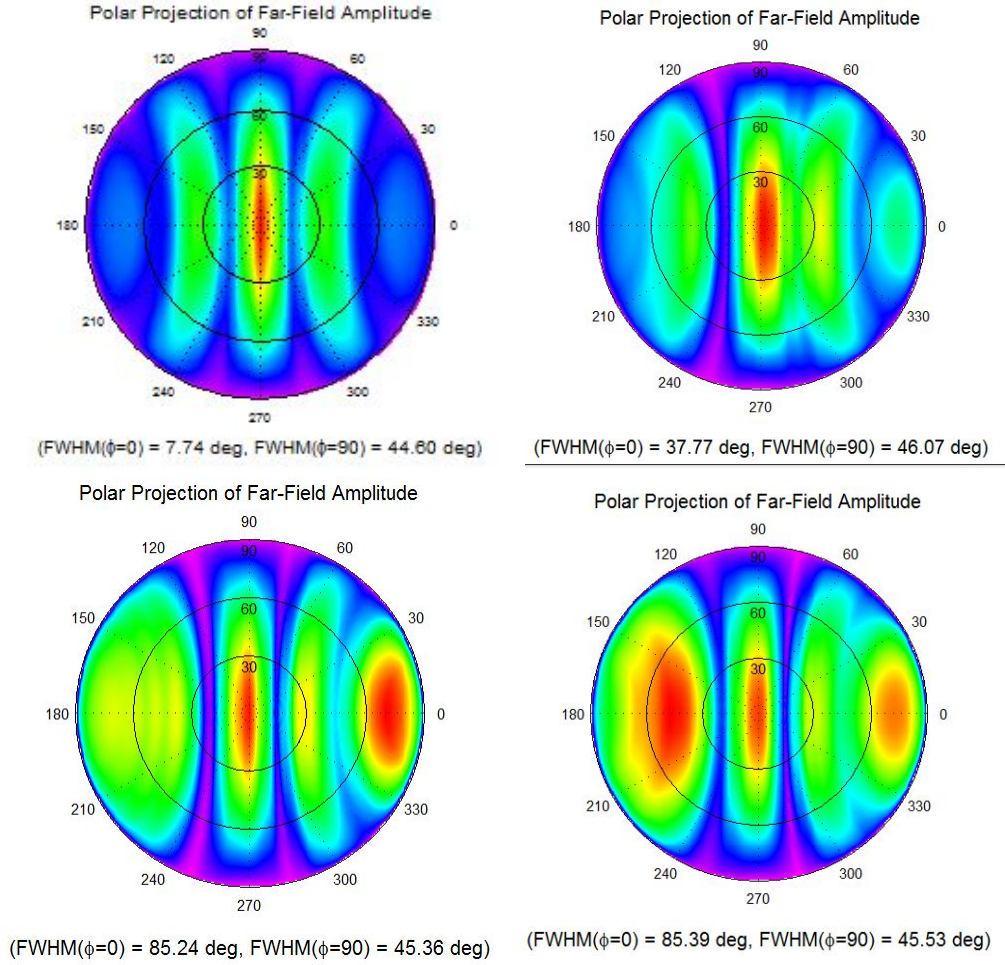


Figure 3.17: **Top**: far-field distribution obtained with zero relative phase-shift between the branches (left) and with a 30° phase-shift just at IN1. In the former case the result is a symmetrical, three-lobed (narrow) lobe response, whereas in the latter the result is blended. **Bottom**: far-field distributions obtained with random input phase-shift and with just 15° difference at port IN2 to demonstrate the flexibility of the system and its promising characteristics in terms of single-pixel condensed imaging.

of various integrated optical components. This is why the final argument treated in this thesis is an attempt of applying such deep learning methods to study the behaviour of our multi-branch OPA for the implementation of condensed imaging.

3.6 A Machine Learning approach to the coupler design and the control of far-field profile

The final section of this chapter is dedicated to the attempt of developing a Deep Neural Network (DNN) to automatize integrated components optimization and to study the

complex relation between the output far-field distribution emitted by our device and the phase-shifts forced on the different branches. As shown in the previous section, it is not simple to determine the 8 control currents required to obtain a requested far field distribution. The basic idea is to train a DNN in order to fix the phase-shift to force the wanted far-field pattern needed for condensed sensing. Moreover, the design of the splitter and the MMI require a remarkable amount of time- and resources- consuming simulations. DNN approaches have been recently proposed for the design and control of Silicon based PIC. In order to become familiar with this approach we tried to reproduce the results that can be found in two recent articles ([32, 33]) about the design and optimization of a nano-structured power splitter at $1.55\ \mu\text{m}$. The experience gained with this exercise will be important not only for the design of new components, but also for the study and design of an efficient far field control strategy. In [32, 33], the analyzed structure is a normal 3-port MMI splitter in standard fully-etched SOI technology. The central square region is characterized by the possible presence of a set of 400 (in a 20×20 field) Silica holes etched in it, in order to minimize the back reflected power and allow for tunable splitting proportions. The system is fully characterized by the definition of a 20×20 matrix (HM) fixing

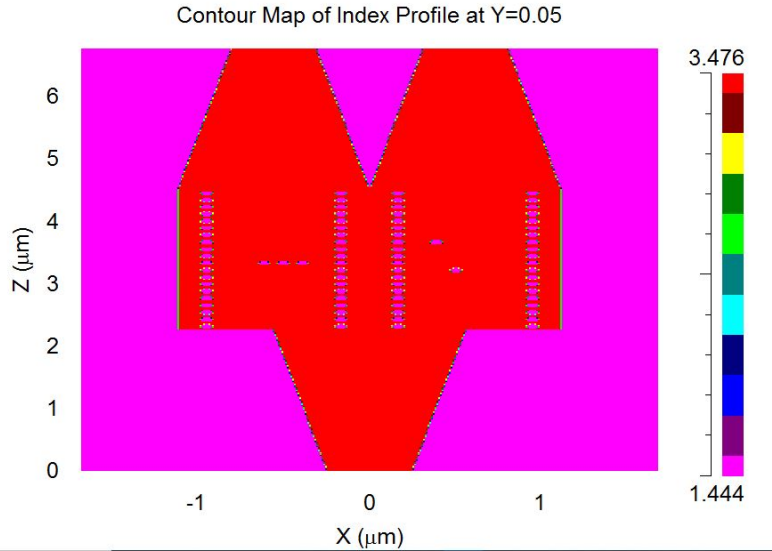


Figure 3.18: The 1-to-2 nano-structured MMI with programmed presence of silica holes in the central splitting region.

the presence or less of the related hole (see figure 3.18 for clarity). In [32] the so-called forward design problem is discussed, namely the training of a DNN with a sufficiently large amount of input specifics (HM) and results (transmission coefficients at the two output ports) to be able to predict with a sufficient degree of confidence the results of a new HM specific. Subsequently the so-called inverse design problem it is presented, that is the definition of the HM given the wanted transmission coefficients at the two output ports, being the interesting mechanism from a design point of view. We tried to reproduce only the first problem since it is a fundamental step also in the definition of the inverse design mechanism.

To do that it is necessary to create a sufficiently large amount of input and output data to

explore in a sufficiently random manner the configuration space of our geometry. By means of a MATLAB computer program we were able to define automatically the geometries to test via an FDTD simulation in the RSoft CAD suite (A.2). The simulation output is a collection of 400 zeros or ones representing the relative absence or presence of the silica holes in silicon, followed by 11 computed transmission coefficients for each output in the wavelength range $1.45\ \mu\text{m}$ - $1.65\ \mu\text{m}$. The complete data collection was composed by 3000 sets of the above-mentioned data. With the extensive specifics found in [32] and the help of the OPTCOM group of the Department of Electronics and Telecommunications of the Politecnico di Torino we were able to train and test a NN for the forward design. In particular from the 3000 simulation results above-mentioned, 70% was used as training material, whereas the other 30% was used as testing set. The trained NN achieved an accuracy of 99.9% for single value prediction and a value just shy of 99.9% for the prediction of the whole spectrum together.

After such a challenging application we tried to apply the same methodology to the control of the far field profile. The goal is to have an algorithm able to fix the phase-shift of each branch to obtain the requested field distribution at the output (inverse design). To do that we focused on the forward problem, that is being able to predict the final far-field distribution for a pseudo-random phase-shift configuration without the need for a time consuming BeamPROP simulation. Similarly to what was done previously, there is the need to generate a large data-set to train and test the NN. Each set of data will be composed by 8 randomly picked phase-shifts in the range 0° - 360° and by the field intensities at some interesting angle. The BeamPROP simulations were automatically managed by a MATLAB program in charge of invoking RSoft and perform the computation with the randomly picked phases. At the end of each simulation an automated process was used to extract the data of interest in the resulting '*.far' file (A.3). With reference for example to figure 3.17 the fields at $\phi = 0^\circ$ and $\phi = 180^\circ$ for all the values of θ were selected and saved in a specific 'Results' file, discarding all the other values. In such a way we were able to record the field intensity just in front of the output waveguide.

By running the MatLab program (A.3) we were able to obtain 6000 sets of data, subsequently fed to another Matlab program (A.4) in which it is trained and tested a NN algorithm. In figure are reported some results obtained by running the algorithm with 70% of the data as training data and the remaining ones as tests. The final RMSE converges to approximately 17%.

3.7 Mask design

The analysis and simulations previously discussed allowed to design a complete GDSII layout mask for the OPA device, shown in figure 3.20. This layout is independent of the production fab and was manually finalized using the free software KLayout [35]. Remark: the central tuning region is shrank by a factor 10 in order to have a more readable mask.

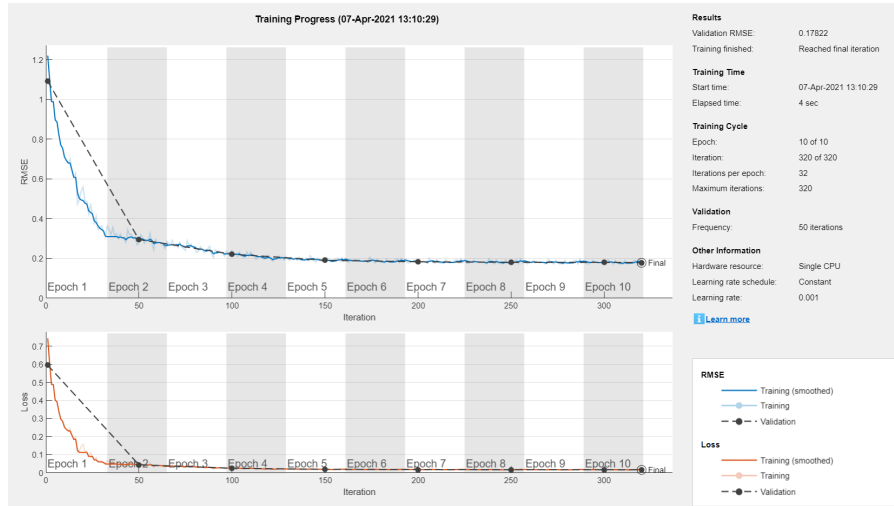


Figure 3.19: Error convergence obtained with a NN algorithm trained with 70% of the obtained data and tested with the other 30%. The RMSE converges to approximately 17%

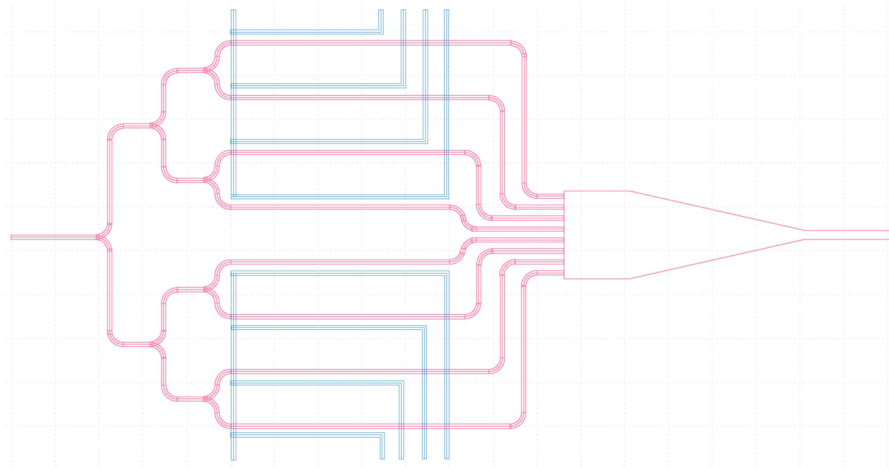


Figure 3.20: Layout mask for the designed OPA device. Red: optical Silicon waveguides; blue: electrical connections. The central thermal-tuning region is 10 times shorter for better readability.

Conclusions

This is the end of my thesis work, in which I had the opportunity to examine in depth the Silicon Photonics integrated biosensors field. In particular I went through some different applications based on evanescent field sampling like the detection of hazardous gaseous compounds and specific molecular interactions. Moreover I decided to focus my attention on the design and optimization of beam-steering and beam-shaping structures with specific application in the bio-imaging field.

Indeed in the last chapter we have completed the design of the basic building blocks needed for the implementation of an OPA. We have been able to fix the geometrical and physical parameter needed for its definition. We have succeeded in designing a structure that can be employed in an imaging system based on single pixel. Such a system is based on the reconstruction of an image by interrogating the target with a spatially resolved field and by collecting the correlated intensity on a single-pixel detector. The advantage of this approach is the possibility to resolve a multi-pixel image faster than with the standard scanning mechanism [31]. In our case the system is thought to be working with back-reflected light (as the detector will be placed close to the "antenna") but in literature articles can be found proving the capability of this type of systems also with transmitted and fluorescent light [30]. Concerning the scan technique, the imaging process can be implemented with different strategies. Raster-scan strategy represent a first basic, sub-optimal idea: each measurement provides information about a single pixel of the image. In order to reduce the number of tests to faithfully reconstruct the image, compressing sensing algorithm are often implemented, made possible by testing the target with pseudo-random field-distributions and further post-processing computations [31]. This topic is far from the objective of this thesis, however what we have demonstrated is the possibility to implement a system that can be used in this direction. In [30] an architecture is proposed similar to ours together with encouraging results concerning its capabilities. Indeed in the same article an OPA structure is designed very similar to the one proposed in this thesis (actually it is a very common solution in single-pixel imaging systems) with a substantial difference in the projecting system. As a matter of fact in [31] the output of the different phase-shifted branches rearranged in a 2D array and coupled to a multi-mode fiber responsible for target illumination. In our system the output once again consists on a multi-mode guiding segment, since this is the key for generating a pseudo-random field distribution on the target. Furthermore now we have trained a machine learning algorithm able to rapidly compute the far-field distribution given a random phase-shift input, being the first step for the implementation of a machine able to perform the inverse calculation and compute the phases once the particular needed pattern is fixed by the chosen condensed sensing

algorithm.

Appendix A

MATLAB programs

A.1 Dispersion relations of a slab waveguide and modal functions

```
1 close all
2 clear
3 syms x
4 nc=1.45; %cladding index
5 ns=1.45; %substrate index
6 nf=3.45; %core/film index
7 d=2e-6; %flim thickness, mm
8 Npt=1e3; %Number of points
9 %%%%%%%%%%%%%%%%%%%%%%%%%%%%%%%%%%%%%%%%%%%%%%%%%%%%%%%%%%%%%%%%%%%%%%%%%%
10 c=3e8; %speed of light, m/s
11 neff=linspace(ns(1,1),0.999*nf,Npt);
12
13 omegaTE=@(neff,nu)(atan(sqrt(((neff.^2)-(ns^2))./((nf^2)-(neff.^2)))))+atan(sqrt(((neff.^2)-(nc^2))./((nf^2)-(neff.^2))))+pi*nu)./(d*sqrt((nf^2)-(neff.^2))/c);
14 %plot the dispersion relations
15 figure
16 for nu=0:4 %Main loop
17 plot(omegaTE(neff,nu)*sqrt((nf^2)-(ns(1,1)^2))*d/c,neff,'r','LineWidth',1)
18 xline(2*pi*sqrt((nf^2)-(ns^2))*d/4e-6,'g','LineWidth',1.5);
19 xlabel('V')
20 ylabel('n_{eff}')
21 hold on
22 end
23 xlim([0 25])
24 ylim([ns nf])
25 grid minor
```

```

26 neff0=3.15; %reference refractive index
27 nu0=0;
28
29 %% TE modeal functions
30 %definition of the characteristic constants
31 omega0=omegaTE(neff0, nu0);
32 V0TE=omega0*sqrt((nf^2)-(ns^2))*d/c;
33 k0=omega0/c;
34 %propagation constants
35 kxc=k0*psqrt((nc^2)-neff0^2);
36 kxs=k0*psqrt((ns^2)-neff0^2);
37 kxf=k0*psqrt((nf^2)-neff0^2);
38 kz=k0*neff0;
39 %definition of the region of interest
40 zmin=10/abs(kxs);
41 zmax=10/abs(kxc);
42 zleft=linspace(-zmin, 0, Npt/3+1);
43 zmiddle=linspace(0, d, Npt/3+1);
44 zright=linspace(d, d+zmax, Npt/3+1);
45
46 %characteristic impedance definitions
47 ZinfTEf=omega0*4e-7*pi/kxf;
48 ZinfTEc=omega0*4e-7*pi/kxc;
49 ZinfTEs=omega0*4e-7*pi/kxs;
50 ZinfTEt=omega0*4e-7*pi/kz;
51
52 %Fresnel reflection coefficient definition
53 GaBmRTE=(kxf-kxc)/(kxf+kxc);
54 GaApRTE=GaBmRTE*exp(-2i*kxf*d);
55 GaApLTE=1/GaApRTE;
56
57 %voltage and current computations
58 psiTE=-angle(1+1/GaApLTE);
59 VpAp=solve(abs(x)^2*abs(1+GaApLTE)^2/(2*abs(kxs))+d*abs(x)^2*(1+
    abs(GaApRTE)^2)+abs(x)^2*abs(1+GaBmRTE)^2/(2*abs(kxc))+2*abs(x)
    ^2*d*sinc(kxf*d/pi)*(real(GaApRTE)*cos(kxf*d)-imag(GaApRTE)*
    sin(kxf*d))=1, x);
60 VpAp=VpAp*exp(1i*psiTE);
61 VmApTE=GaApRTE*VpAp;
62 VmAmTE=(1+GaApLTE)*VmApTE;
63 VpBmTE=VpAp*exp(-1i*kxf*d);
64 VpBpTE=(1+GaBmRTE)*VpBmTE;
65 VsTE=VmAmTE*exp(+1i*kxs*zleft);
66 VfTE=VpAp*exp(-1i*kxf*zmiddle)+VmApTE*exp(1i*kxf*zmiddle);
67 VcTE=VpBpTE*exp(-1i*kxc*(zright-d));
68 IsTE=-VmAmTE*exp(+1i*kxs*zleft)/ZinfTEs;

```

```

69 IfTE=(VpAp*exp(-1i*kxf*zmiddle)-VmApTE*exp(1i*kxf*zmiddle))/
    ZinfTEf;
70 IcTE=VpBpTE*exp(-1i*kxc*(zright-d))/ZinfTEc;
71
72 %plots of the modal functions
73 figure('Name', sprintf('TE polarization mode functions for \nu=%d
    @ neff=%0.2f & V=%0.3f', nu0, neff0, V0TE))
74 subplot(1,3,1)
75 plot(zleft, VsTE, 'k')
76 hold on
77 plot(zmiddle, VfTE, 'k')
78 plot(zright, VcTE, 'k')
79 grid minor
80 title('{E_y(x)}')
81 xlabel('x(m)')
82 xline(0, 'r');
83 xline(d, 'r');
84
85 subplot(1,3,2)
86 plot(zleft, -VsTE/ZinfTEt, 'k')
87 hold on
88 plot(zmiddle, -VfTE/ZinfTEt, 'k')
89 plot(zright, -VcTE/ZinfTEt, 'k')
90 grid minor
91 title('{H_x(x)}')
92 xlabel('x(m)')
93 xline(0, 'r');
94 xline(d, 'r');
95
96 subplot(1,3,3)
97 plot(zleft, imag(IsTE), 'k')
98 hold on
99 plot(zmiddle, imag(IfTE), 'k')
100 plot(zright, imag(IcTE), 'k')
101 grid minor
102 title('{H_z(x)}')
103 xlabel('x(m)')
104 xline(0, 'r');
105 xline(d, 'r');

```

A.2 Program to create the data-set for nanostructured splitter

```

1 clear
2 N=20;           %Number of holes per row
3 NumRuns=3000;  %Number of simulations
4 SourceFileName='Source.ind'; %Simulation file source
5 Workers=4;     %Number of parallel pools
6 %%%%%%%%%%%%%%
7 Results=cell(NumRuns,1);
8 %creation of a parpool
9 poolobj=gcp('nocreate');
10 if isempty(poolobj) || poolobj.NumWorkers ~=Workers
11     poolobj =parpool(Workers);
12 end
13 %Parallel execution
14 spmd
15     LocalRuns=round(NumRuns/Workers);
16     ResultsFilename=sprintf('Results%02d.txt',labindex);
17     hFile=fopen(ResultsFilename,'w');
18     for k=1+((labindex-1)*LocalRuns):LocalRuns+((labindex-1)*
19         LocalRuns)
20         fprintf('Worker %d, simulation %d of %d started\n',
21             labindex,k,NumRuns);
22         A=rand(N,N)>0.5; %random matrix defining presence of
23             holes
24         Prefix=sprintf('Target%04d',k);
25         %generation of a geometry according to the random A
26             matrix
27         SimulationFileName=sprintf('%s.ind',Prefix);
28         CreateGeometry(A,SourceFileName,SimulationFileName);
29         %RSoft call
30         ExecuteRSoft(SimulationFileName,Prefix);
31         %read the results
32         M1=ReadResults(Prefix,1);
33         M2=ReadResults(Prefix,2);
34         %pack results in the final cell
35         Results=[reshape(A,1,N*N),M1,M2];
36         delete([Prefix '.*']); %delete all the files to save
37             save space
38         pause(0.01);
39         %generation of a result file for each worker to improve
40             stability
41         writematrix(Results,sprintf('Result%04d.txt',k),'
42             Delimiter','tab');

```

```

36     fprintf(hFile , '%0.8g\t' ,Results);
37     fprintf(hFile , '\r\n');
38     fprintf('Simulation %d of %d done!\n' ,k ,NumRuns);
39     end
40     fclose (hFile);
41 end
42 %Create the RSoft input file
43 function CreateGeometry(M, SourceFilename , DestinationFileName)
44 z=0;
45 fSource = fopen(SourceFilename , 'r');
46 fDestination = fopen(DestinationFileName , 'w');
47 tline=fgetl(fSource);
48 while strcmp(tline , 'launch_field' , 12)==0 && ...
49     not( feof(fSource))
50     if strcmp(tline , 'segment' ,7) || ...
51         strcmp(tline , 'time_monitor' ,12)
52         z=z+1;
53     end
54     fprintf(fDestination , '%s\n' ,tline);
55     tline=fgetl(fSource);
56 end
57 for i=1:size(M,1)
58     for j=1:size(M,2)
59         if M(i ,j)==1
60             z=z+1;
61             fprintf(fDestination ,...
62                 'lens %d\n\tiscircle = 1\n\ttrfront = (2*R)/2\n\
63                 trback = -(2*R)/2\n\tbegin.x = -1.125+(%f*DX+%
64                 d*R)\n\tbegin.z = %f*DX+%d*R rel end segment
65                 1\n\tbegin.width = 2*R\n\end lens\n\n' ,z ,i
66                 -0.5 ,2*i -1 ,j -0.5 ,2*j -1);
67         end
68     end
69 end
70 if not( feof(fSource))
71     while not( feof(fSource))
72         fprintf(fDestination , '%s\n' ,tline);
73         tline=fgetl(fSource);
74     end
75 end
76 fclose (fSource);
77 fclose (fDestination);
78 end
79 %Read results from RSoft output file
80 function M=ReadResults(Prefix ,Port)
81 Filename=sprintf(' %s_Port%d_pow.dmn' ,Prefix ,Port);

```

```
78 M=readmatrix(FileName, 'FileType', 'text');
79 M=M(:,2) .';
80 end
81 %Execte RSoft from command line
82 function ExecuteRSoft(SourceFileName, Prefix)
83 CommandString=sprintf('fullwave -hide %s prefix=%s wait=0',
    SourceFileName, Prefix);
84 system(CommandString);
85 pause(0.01);
86 end
```

A.3 Program to create the data-set for far-field study

```

1 clear
2 N=8; %Number of phases to tune
3 NumRuns=6000; %Number of simulations to perform
4 SourceFileName='Target.ind'; %Target filename
5 Workers=2; %Number of parallel worker in the pool
6 %%%%%%%%%%
7 Results=cell(NumRuns,1); %Destination cells
8 poolobj=gcp('nocreate'); %Get current pool
9 %create a pool if not already existing
10 if isempty(poolobj) || poolobj.NumWorkers ~=Workers
11     poolobj =parpool(Workers);
12 end
13 %parallel code
14 spmd
15     %Number of simulations per worker
16     LocalRuns=round(NumRuns/Workers);
17     ResultsFilename=sprintf('Results%02d.txt',labindex);
18     hFile=fopen(ResultsFilename,'w');
19     %Iteration inside a worker
20     for k=1+((labindex-1)*LocalRuns):LocalRuns+((labindex-1)*
21         LocalRuns)
22         fprintf('Worker %d, simulation %d of %d started\n',
23             labindex,k,NumRuns);
24         %Generate random phase
25         phi_rand=360.*rand(N,1);
26         Prefix=sprintf('Target%04d',k);
27         %Single simulation source filename
28         SimulationFileName=sprintf('%s.ind',Prefix);
29         %Create the source file
30         CreateGeometry(SourceFileName,SimulationFileName);
31         % RSoft call
32         ExecuteRSoft(SimulationFileName, Prefix, phi_rand);
33         % read the results
34         M=ReadResults(Prefix);
35         %pack results in the final cell
36         Results=[reshape(phi_rand,1,N) M];
37         delete([Prefix '.*']);
38         pause(0.01);
39         writematrix(Results, sprintf('Result%04d.txt',k), '
40             Delimiter','tab');
41         fprintf(hFile,'%0.8g\t',Results);
42         fprintf(hFile,'\r\n');
43         fprintf('Simulation %d of %d done!\n',k,NumRuns);
44     end
45 end

```

```

42     fclose(hFile);
43 end
44
45 %Create the .ind file for the RSoft simulation
46 function CreateGeometry(SourceFilename, DestinationFileName)
47 fSource = fopen(SourceFilename, 'r');
48 fDestination = fopen(DestinationFileName, 'w');
49 tline=fgetl(fSource);
50 while not(feof(fSource))
51     fprintf(fDestination, '%s\n', tline);
52     tline=fgetl(fSource);
53 end
54 fclose(fSource);
55 fclose(fDestination);
56 end
57
58 %Read results from RSoft file
59 function M=ReadResults(Prefix)
60 Filename=sprintf('%s.far', Prefix);
61 fid=fopen(Filename, 'r');
62 i=0;
63 while not(feof(fid))
64     tline=fgetl(fid);
65     i=i+1;
66     if i==5
67         M1=sscanf(tline, '%f').';
68     end
69     if i==95
70         M2=sscanf(tline, '%f').';
71     end
72 end
73 fclose(fid);
74 M=[M2((length(M2)-1):-2:1) M1(1:2:length(M1))];
75 end
76 %Execute RSoft from command line
77 function ExecuteRSoft(SourceFileName, Prefix, phi_rand)
78 CommandString=sprintf('bsimw32 -hide %s prefix=%s wait=0 phil=%f
    phi2=%f phi3=%f phi4=%f phi5=%f phi6=%f phi7=%f phi8=%f',
    SourceFileName, Prefix, phi_rand(1), phi_rand(2), phi_rand(3),
    phi_rand(4), phi_rand(5), phi_rand(6), phi_rand(7), phi_rand(8));
79 system(CommandString);
80 pause(0.01);
81 end

```

A.4 Program for the training and testing of a NN for far-field computation

```

1 %Script for the training of the NN for the far field control
2 %Requires MATLAB>=2021a
3 %Name of file containing the phases in the first columns and
4 %the far field samples in the following columns
5 Filename='Results01.txt';
6 %Number of paths used to thermally tune the field pahse
7 NumberOfPhaseControlWgs=8;
8 %Angles of the Far Field samples to consider.
9 FarFieldAngles=[-90, -45, 0, 45, 90];
10 %%%%%%%%%%%%%%%%%%%%%%%%%%%%%%%%%%%%%%%%%%%%%%%%%%%%%%%%%%%%%%%%%%%%%%%%%%
11 %Read all data
12 A=readmatrix(Filename);
13 %Extract phases, normalize between 0(0 degrees) and 1 (360
    degrees)
14 Phases=A(:,1:NumberOfPhaseControlWgs)/360;
15 %Extract Far Field samples
16 NumberOfFarFieldSamples=size(A,2)-NumberOfPhaseControlWgs;
17 FarFields=A(:,NumberOfPhaseControlWgs+1:end);
18 %Normalize with respect to simulation maximum
19 FarFields=FarFields./max(FarFields(:));
20 %Convert angles (-180 to +180) to indices (1 to
    NumberOfFarFieldSamples)
21 FarFieldIndices=round((FarFieldAngles+180)/360*(
    NumberOfFarFieldSamples-1))+1;
22 %Remove indices outside the bounds
23 FarFieldIndices(...
24     FarFieldIndices<1 | ...
25     FarFieldIndices>NumberOfFarFieldSamples ...
26     )=[];
27 %Remove potentially duplicated indices
28 FarFieldIndices=unique(FarFieldIndices);
29 %Only keep the Far Field samples for the requested phase
30 FarFields=FarFields(:,FarFieldIndices);
31 %Number of NN features
32 NumberOfFeatures=NumberOfPhaseControlWgs;
33 %Number of NN outputs
34 NumberOfOutputs=size(FarFields,2);
35 %Divide between Training set and Test set
36 TrainingSize=0.7*size(Phases,1);
37 PhasesTrain=Phases(1:TrainingSize,:);
38 FarFieldsTrain=FarFields(1:TrainingSize,:);
39 PhasesTest=Phases(TrainingSize+1:end,:);

```

```
40 FarFieldsTest=FarFields(TrainingSize+1:end,:);
41 %Layers for the NN
42 layers = [ ...
43     featureInputLayer(NumberOfFeatures); %raw numerical input
44     fullyConnectedLayer(NumberOfFeatures*2);%connected layer
45     fullyConnectedLayer(NumberOfOutputs); %connected layer
46     regressionLayer]; %regression, no
         categorization
47 %Training options
48 options = trainingOptions('rmsprop', ...
49     'LearnRateDropFactor',0.01, ...
50     'LearnRateDropPeriod',5, ...
51     'MaxEpochs',10, ...
52     'ValidationData',{PhasesTest, FarFieldsTest}, ...
53     'MiniBatchSize',128, ...
54     'Plots','training-progress');
55 %Create the NN
56 net = trainNetwork(PhasesTrain, FarFieldsTrain, layers, options);
```

Bibliography

- [1] Synopsys tools <https://www.synopsys.com>
- [2] Banica Florinel-Gabriel, *Chemical sensors and biosensors : fundamentals and applications* .
- [3] Caterina Ciminelli, Francesco Dell'Olio, Donato Conteduca, Mario Nicola Armenise in 'IET journal', *Silicon photonic biosensors*
- [4] Caterina Ciminelli, Clarissa Martina Campanella, Francesco Dell'Olio, Carlo Edoardo Campanella, Mario Nicola Armenise *Label-free optical resonant sensors for biochemical applications*
- [5] David Thomson, Aaron Zilkie, John E Bower, Tin Komljenovic, Graham T Reed, Laurent Vivien, Delphine Marris-Morini, Eric Cassan, Léopold Virost, Jean-Marc Fédéli, Jean-Michel Hartmann, Jens H Schmid, Dan-Xia Xu, Frédéric Boeuf, Peter O'Brien, Goran Z Mashanovich and M Nedeljkovic, *Roadmap on silicon photonics*, Journal of Optics
- [6] Richard A Soref et al 2006 J. Opt. A: Pure Appl. Opt. 8 840
- [7] M. Nedeljkovic, A. Z. Khokhar, Y. Hu, X. Chen, J. Soler Penades, S. Stankovic, H. M. H. Chong, D. J. Thomson, F. Y. Gardes, G. T. Reed, and G. Z. Mashanovich, *Silicon photonic devices and platforms for the mid-infrared*
- [8] Sergio Nicoletti, Jean-Marc Fédéli, Maryse Fournier, Pierre Labeye, Pierre Barritault, Adrien Marchant, Alain Glière, Alexandre Teulle, Jean-Guillaume Coutard, Laurent Duraffourg, *Miniaturization of mid-IR sensors on Si: challenges and perspectives* , Proc. SPIE 10923, Silicon Photonics XIV, 109230H (4 March 2019);
- [9] Patrick Steglich, *Silicon-on-Insulator Slot Waveguides: Theory and Applications in Electro-Optics and Optical Sensing*
- [10] Enxiao Luan, Hossam Shoman, Daniel M. Ratner, Karen C. Cheung and Lukas Chrostowski, *Silicon Photonic Biosensors Using Label-Free Detection*, 2018 Sensors
- [11] Adrián Fernández Gavela, Daniel Grajales García, Jhonattan C. Ramirez and Laura M. Lechuga, *Last Advances in Silicon-Based Optical Biosensors*, 2016 Sensors
- [12] Patrick Steglich, Marcel Hülsemann, Birgit Dietzel and Andreas Mai, *Optical Biosensors Based on Silicon-On-Insulator Ring Resonators: A Review*, 2019 Sensors
- [13] Andreas Hänsel and Martijn J. R. Heck, *Feasibility of Telecom-Wavelength Photonic Integrated Circuits for Gas Sensors*, 2018, Sensors
- [14] Christian Ranacher, Cristina Consani, Andreas Tortschanoff, Reyhaneh Jannesari, Markus Bergmeister, Thomas Grille, Bernhard Jakoby, *Mid-infrared absorption gas sensing using a silicon strip waveguide* Sensors and Actuators A: Physical, 2018 Elsevier

-
- [15] Andreas Hänsel, Martijn J. R. Heck, *Feasibility of Telecom-Wavelength Photonic Integrated Circuits for Gas Sensors*, 2018 Sensors
- [16] Liaquat Ali, Mahrukh Khan, Mahmood Uddin Mohammed, Abdul Hamid B. Yousuf, Masud H Chaudhry, *High Quality Silicon Photonics Optical Ring Resonator Biosensor Design*, 2018, University of Missouri-Kansas City
- [17] Adam L. Washburn, Matthew S. Luchansky, Adrienne L. Bowman, and Ryan C. Bailey, *Quantitative, Label-Free Detection of Five Protein Biomarkers Using Multiplexed Arrays of Silicon Photonic Microring Resonators*, 2010, Letters to Analytical Chemistry
- [18] Francesco Dell'Olio, Donato Conteduca, Caterina Ciminelli, and Mario Nicola Armenise, *New ultrasensitive resonant photonic platform for label-free biosensing*, 2015, Optical Society of America
- [19] Daoxin Dai, *Highly sensitive digital optical sensor based on cascaded high-Q ring-resonators*, 2009, Optical Society of America
- [20] YONG LIU, YANG LI, MINGYU LI, AND JIAN-JUN HE, *High-sensitivity and wide-range optical sensor based on three cascaded ring resonators*, 2017, Optical Society of America
- [21] A.B. González-Guerrero, S. Dantea, Daphné Duvala, J. Osmond, Laura M. Lechuga, *Advanced photonic biosensors for point-of-care diagnostics*, 2011, Elsevier
- [22] Kirill Zinoviev, Laura G. Carrascosa, Jose Sanchez del Rio, Borja Sepulveda, Carlos Dominguez, and Laura M. Lechuga, *Silicon Photonic Biosensors for Lab-on-a-Chip Applications*, 2008, Hindawi Publishing Corporation, Advances in Optical Technologies
- [23] B Sepulveda, J Sanchez del Rio, M Moreno, F J Blanco, K Mayora, C Dominguez and L M Lechuga, *Optical biosensor microsystems based on the integration of highly sensitive Mach-Zehnder interferometer devices*, 2005, Optical Society of America
- [24] Qing Liu, Xiaoguang Tu, Kyung Woo Kim, Jack Sheng Kee, Yong Shin, Kyungsup Han, Yong-Jin Yoon, Guo-Qiang Lo, Mi Kyoung Park, *Highly sensitive Mach-Zehnder interferometer biosensor based on silicon nitride slot waveguide*, 2013, Elsevier, Sensors and Actuators B: Chemical
- [25] Soichiro Yoshida, Shintaro Ishihara, Taro Arakawa and Yasuo Kokubun, *Highly sensitive optical biosensor based on silicon-microring-resonator-loaded Mach-Zehnder interferometer*, 2016, Japanese Journal of Applied Physics
- [26] L. TOMBEZ, E. J. ZHANG, J. S. ORCUTT, S. KAMLAPURKAR, AND W. M. J. GREEN, *Methane absorption spectroscopy on a silicon photonic chip*, 2017, Journal of Optical Society of America
- [27] Floria Ottonello-Briano, Carlos Errando-Herranz, Henrik Rödjegård, Hans Martin, Hans Sohlström, AND Kristinn B. Gylfason, *Carbon dioxide absorption spectroscopy with a mid-infrared silicon photonic waveguide*, 2020, Journal of Optical Society of America
- [28] Babita Kumari, R.K. Varshney, B.P. Pal, *Design of chip scale silicon rib slot waveguide for sub-ppm detection of N₂O gas at mid-IR band*, 2017, Elsevier, Sensors and Actuators B: Chemical
- [29] Mathias Prost, Yi-Chun Ling, Semih Cakmakyapan, Yu Zhang, Kaiqi Zhang, Junjie Hu, Yichi Zhang, S. J. Ben Yoo, *Solid-State MWIR Beam Steering Using Optical Phased Array on Germanium-Silicon Photonic Platform*, 2019, IEEE Photonics Journal

- [30] Taichiro Fukui, Yusuke Kohno, Rui Tang, Yoshiaki Nakano, and Takuo Tanemura , *Single-Pixel Imaging Using Multimode Fiber and Silicon Photonic Phased Array*, 2021, JOURNAL OF LIGHTWAVE TECHNOLOGY
- [31] Matthew P. Edgar, Graham M. Gibson and Miles J. Padgett, *Principles and prospects for single-pixel imaging*, 2019, Nature Photonics
- [32] Kojima, Keisuke; TaherSima, Mohammad; Koike-Akino, Toshiaki; Jha, Devesh; Tang, Yingheng; Wang, Ye; Parsons, Kieran, *Deep Neural Networks for Inverse Design of Nanophotonic Devices*, 2021, IEEE Journal of Lightwave Technology
- [33] Kojima, Keisuke; TaherSima, Mohammad; Koike-Akino, Toshiaki; Jha, Devesh; Tang, Yingheng; Wang, Ye; Parsons, Kieran, *Deep Neural Network Inverse Design of Integrated Nanophotonic Devices*, 2018
- [34] JINGWEN HE, TAO DONG, AND YUE XU, *Review of Photonic Integrated Optical Phased Arrays for Space Optical Communication*, 2020, IEEE Access
- [35] KLayout - Mask layout editor <https://www.klayout.de/>